NAVAL POSTGRADUATE SCHOOL
Monterey, California

THESIS

MODEL-DATA COMPARISON OF SHALLOW WATER ACOUSTIC REVERBERATION IN THE EAST CHINA SEA

by

Robert M. Hill

September 2003

Thesis Advisor:	Kevin B. Smith
Second Reader:	Daphne Kapolka

Approved for public release; distribution is unlimited

THIS PAGE INTENTIONALLY LEFT BLANK

REPORT DOCUMENTATION PAGE			Form Approved OMB No. 0704-0188
Public reporting burden for this collection of information is estimated to average 1 hour per response, including the time for reviewing instruction, searching existing data sources, gathering and maintaining the data needed, and completing and reviewing the collection of information. Send comments regarding this burden estimate or any other aspect of this collection of information, including suggestions for reducing this burden, to Washington headquarters Services, Directorate for Information Operations and Reports, 1215 Jefferson Davis Highway, Suite 1204, Arlington, VA 22202-4302, and to the Office of Management and Budget, Paperwork Reduction Project (0704-0188) Washington DC 20503.			
1. AGENCY USE ONLY *(Leave blank)*	**2. REPORT DATE** September 2003	**3. REPORT TYPE AND DATES COVERED** Master's Thesis	
4. TITLE AND SUBTITLE: Model-Data Comparison of Shallow Water Acoustic Reverberation in the East China Sea			**5. FUNDING NUMBERS**
6. AUTHOR(S) Robert M. Hill			
7. PERFORMING ORGANIZATION NAME(S) AND ADDRESS(ES) Naval Postgraduate School Monterey, CA 93943-5000			**8. PERFORMING ORGANIZATION REPORT NUMBER**
9. SPONSORING /MONITORING AGENCY NAME(S) AND ADDRESS(ES) N/A			**10. SPONSORING/MONITORING AGENCY REPORT NUMBER**
11. SUPPLEMENTARY NOTES The views expressed in this thesis are those of the author and do not reflect the official policy or position of the Department of Defense or the U.S. Government.			
12a. DISTRIBUTION / AVAILABILITY STATEMENT Approved for public release; distribution is unlimited			**12b. DISTRIBUTION CODE**

13. ABSTRACT ***(maximum 200 words)***

In this thesis, the Monterey-Miami Parabolic Equation (MMPE) model is used to generate predictions from numerical analysis of the reverberation loss structure and peak vertical correlation structure generated by the water/bottom interface, the bottom/sub-bottom interface, and the bottom volume for a shallow water environment. These predictions are then compared to the peak vertical correlation analysis of recorded data collected in an actual shallow water environment similar to the modeled environment. This experimental data was recorded by a 32-element vertical line array (VLA) that recorded the reverberant return generated by charges detonated over the continental shelf in the East China Sea as part of ASIAEX. A comparison is made between predictions and recorded data by analyzing trends in peak vertical correlation with decreasing bandwidth. The influences of interface roughness, bottom volume perturbations, and water volume turbulence on peak vertical correlation is also determined.

14. SUBJECT TERMS Shallow water reverberation, reverberation pressure levels, coherence, peak vertical correlations, East China Sea, MMPE			**15. NUMBER OF PAGES** 89
			16. PRICE CODE
17. SECURITY CLASSIFICATION OF REPORT Unclassified	**18. SECURITY CLASSIFICATION OF THIS PAGE** Unclassified	**19. SECURITY CLASSIFICATION OF ABSTRACT** Unclassified	**20. LIMITATION OF ABSTRACT** UL

NSN 7540-01-280-5500 Standard Form 298 (Rev. 2-89)
Prescribed by ANSI Std. 239-18

THIS PAGE INTENTIONALLY LEFT BLANK

Approved for public release; distribution is unlimited

MODEL-DATA COMPARISON OF SHALLOW WATER ACOUSTIC REVERBERATION IN THE EAST CHINA SEA

Robert M. Hill
Lieutenant, United States Navy
B.S., University of California, Los Angeles, 1996

Submitted in partial fulfillment of the
requirements for the degree of

MASTER OF SCIENCE IN ENGINEERING ACOUSTICS

from the

NAVAL POSTGRADUATE SCHOOL
September 2003

Author: Robert M. Hill

Approved by: Kevin B. Smith
Thesis Advisor

Daphne Kapolka
Second Reader

Kevin B. Smith, Chairman
Engineering Acoustics Academic Committee

THIS PAGE INTENTIONALLY LEFT BLANK

ABSTRACT

In this thesis, the Monterey-Miami Parabolic Equation (MMPE) model is used to generate predictions from numerical analysis of the reverberation loss structure and peak vertical correlation structure generated by the water/bottom interface, the bottom/sub-bottom interface, and the bottom volume for a shallow water environment. These predictions are then compared to the peak vertical correlation analysis of recorded data collected in an actual shallow water environment similar to the modeled environment. This experimental data was recorded by a 32-element vertical line array (VLA) that recorded the reverberant return generated by charges detonated over the continental shelf in the East China Sea as part of ASIAEX. A comparison is made between predictions and recorded data by analyzing trends in peak vertical correlation with decreasing bandwidth. The influences of interface roughness, bottom volume perturbations, and water volume turbulence on peak vertical correlation is also determined.

THIS PAGE INTENTIONALLY LEFT BLANK

TABLE OF CONTENTS

LIST OF FIGURES

LIST OF TABLES

THIS PAGE INTENTIONALLY LEFT BLANK

ACKNOWLEDGMENTS

My heartfelt thanks got out to the following (but is far from limited to):

Prof. Kevin Smith- You turned what is already a milestone achievement into a truly rewarding experience. I will always hold you in highest regard as a mentor and a friend.

Prof. Daphne Kapolka- Your time and perspective helped both me and my thesis to reach our full potential.

Prof. Jim Sanders and Steve Baker- My time at NPS and my studies in acoustics would not have been as rewarding without your tutelage.

My wife, Darlene- You have always been and will always be my constant friend and companion.

And lastly, to Ben Burrt for making sound seem cool enough to study.

THIS PAGE INTENTIONALLY LEFT BLANK

I. INTRODUCTION

Amazing advances have been achieved in the implementation of tactical active sonar systems to prosecute the underwater environment since their advent over eight decades ago. In all of this time, however, very little progress has been made in combating the adverse effects that strong reverberation in a shallow water environment has on the effectiveness of these systems. As the United States Navy places an ever-increasing effort on operating in the littoral regions of the world, finding methods to understand, predict, and compensate for the effects of reverberation to increase the performance of underwater detection and tracking systems in the shallow water environment has become more important than ever. To realize such an advance requires a better understanding of the primary mechanisms that generate reverberation in the shallow water environment, the impact of environmental variability on acoustic propagation, and the unique factors of the reverberation returns that may allow signal discrimination by advanced processing techniques.

To study the effects of deep ocean acoustic reverberation, a series of experiments was conducted near the Mid-Atlantic Ridge over a several year span in the early-1990's. This program was known as the Acoustic Reverberation Special Research Project (ARSRP) and was sponsored by the Office of Naval Research (ONR). The results of the data analysis[1], [3], [4] from these experiments showed that the general structure of the measured reverberation often agreed with the predictions that were based on propagation modeling, particularly when high reverberant returns were observed in areas where the acoustic energy interacted strongly with the bottom. This conclusion validated the use of propagation modeling to accurately predict the observed long wavelength reverberation statistics of the two-way transmission loss.

Recently, another such study shifted the focus of reverberation research to the shallow water environment. ONR sponsored this reverberation study as part of the Asian Seas International Acoustic Experiment (ASIAEX), a scientific collaboration between the United States, the People's Republic of China, and Japan, conducted in June of 2001. This experiment was conducted over the shallow continental shelf of the East China Sea.

In this region, a soft bottom layer of sand or mud lies about 100m below the ocean surface, with a harder layer of sand, gravel, or rocks beneath it. Evidence suggests that that the transition between these two layers forms a second distinct interface layer that lies approximately 10m below the water/bottom interface. Recorded data from the reverberation generated by explosive sources and recorded by a 32-element vertical line array (VLA) during this study is available thanks to the efforts of Ji-Xun Zhou of the Georgia Institute of Technology.

In recent years, continuing thesis work[5], [6], [7] has been conducted using the Monterey-Miami Parabolic Equation (MMPE) propagation model[8] to predict the structure of reverberation in a shallow water environment. Smith and Li first introduced the use of this method in 2000.[2] Since then, the model has been updated and improved to more accurately simulate the ocean environment and the effect of its features on acoustic propagation. Such improvements now accurately predict the effects of bottom interface roughness, bottom volume perturbations, and water volume turbulence.

The previous thesis work involved a modeled environment and geometry similar to that observed during the ASIAEX. In this work, a 16-element VLA was modeled to support predictions of both monostatic and bistatic reverberation in a shallow water environment. The element at a depth of 48m was used to act as a source placed in the middle of the water column and all of the elements acted as receivers. The water/bottom interface was set at 100m with a bottom/sub-bottom interface placed 5m below it. The modeled reference environment included bottom and sub-bottom characteristics based on geo-acoustic data taken from the East China Sea provided by James H. Miller and Gopu Potty of the University of Rhode Island and a sound speed profile derived from averaged Current Temperature Depth (CTD) measurements taken from the *R/V Melville* provided by Peter Dahl, Chief Scientist for the East China Sea component of ASIAEX. Within this modeled environment, reverberation analyses were conducted for continuous wave (CW) pulses and broadband pulses for a variety of different environmental variations. To generate these broadband pulses, the MMPE Model was run for 512 frequency bins spanning a 250 Hz bandwidth centered on a frequency of 250 Hz. In these analyses, particular attention was paid to reverberation loss generated by the interfaces and the

bottom volume and the peak vertical correlation of these reverberation loss structures. Some of the significant findings from these previous works are as follows:

- CW analysis was unable to capture the coherent structure of reverberation from the bottom volume due to an inability to properly resolve multi-path effects. As a result, peak vertical correlation analysis was only valid for broadband calculation.
- Peak vertical correlation analysis showed that reverberation from the volume decorrelates more rapidly across the vertical array than reverberation from the water/bottom interface and the bottom/sub-bottom interface.
- Higher reverberation levels are observed with increased roughness of the interface. Peak vertical correlation for the bottom/sub-bottom interface displayed a clear decreasing trend with increased roughness.
- Lower reverberation levels are observed for larger sound speed perturbations in the bottom volume. Despite the presence of this trend, no significant change is observed for the peak vertical correlation for either interface or the bottom volume with larger sound speed perturbations.
- The influence of variations in the sound speed profile (SSP) was insignificant with respect to both reverberation levels and the peak vertical correlation for either interface or the bottom volume.

The objective of this analysis is to expand on the previous work and use the methods developed in them to generate accurate reverberation predictions for the environment observed in ASIAEX. In conducting the numerical analysis, the source will be modified from previous work to more accurately model the explosive charges used in ASIAEX. To account for a larger portion of the acoustic energy generated by a wide band explosive source, a wider frequency bandwidth of 500 Hz centered at 350 Hz as calculated over 1024 frequency bins will be used. The frequency spectrum generated by a Standard Underwater Source (SUS) charge, similar to the charges used in ASIAEX, will also be applied to the numerical analysis instead of the Hanning window frequency

spectrum applied in the previous work. This will be accomplished by applying a modeled SUS charge spectrum as provided by David Knobles of the University of Texas.

The results of the predictions generated by the numerical analysis will then be used as a basis for comparison with the recorded data from ASIAEX. Recent research[13] describes a method in which the spatial coherence of a reverberant signal can yield information regarding the nature of the reverberation - specifically, whether this reverberation is generated at an interface or within the bottom volume. This method exploits changes in spatial coherence with changes in transmitted pulse length, which implies that similar changes can be exploited for different bandwidths when using a broadband source. As a measure of spatial coherence, emphasis will be placed on the peak vertical correlations for both the predicted and recorded signals and how these peak vertical correlations are effected by bandwidth size.

Exploitable changes in spatial coherence are those that display some type of distinct difference between the interfaces and the bottom volume in the behavior of their peak vertical correlation structures as bandwidth is changed. Variations in environmental factors could affect the coherence of the acoustic signal through both direct effects on scatter and indirect effects along the propagation path. If the coherence is significantly affected, a change may then arise in peak vertical correlation structures, which could diminish or destroy exploitable changes in spatial coherence. To determine the influence of direct effects on scatter, variations in roughness for both the water/bottom interface and the bottom/sub-bottom interface and variations in the magnitude of bottom volume sound speed perturbations are generated and the resulting reverberation loss and peak vertical correlations are determined. To examine an indirect effect, variations in water volume sound speed turbulence will be examined in the same fashion. Similar analysis for the direct influences of interface roughness and bottom volume sound speed perturbations has been done in previous work,[7] but not for the source spectrum that will be applied here.

The remainder of this thesis is organized as follows. The second chapter introduces reverberation theory, environmental variation, and the use of spatial coherence for separating and discriminating bottom and surface scatter. Methods for the numerical

implementation of this theory will be discussed in the third chapter. The results of both the numerical analysis and analysis of the recorded data from ASIAEX and their implications are presented in the fourth chapter. The final chapter summarized this work and generates a few suggestions for future work.

THIS PAGE INTENTIONALLY LEFT BLANK

II. THEORY

A. REVERBERATION THEORY

For underwater acoustics applications, the term "reverberation" pertains to the scattering and re-radiation of acoustic energy transmitted from a source by the multitude of non-target-of-interest items in the ocean environment. These items include waterborne elements such as bubbles, marine life (the swim bladders of fish in particular), and the ocean surface. Elements of the ocean bottom such as the sea floor interface and discontinuities in the bottom volume also play a significant factor. In the shallow water environment, it is the effects of this later group that is of particular importance. To better understand the mechanisms by which bottom features contribute to reverberation, the effect of the water/bottom interface, a bottom/sub-bottom interface, and inhomogeneities within the bottom volume are examined.

The scattering mechanisms for reverberation for both a monostatic geometry, in which source and receiver are collocated, and a bistatic geometry, where source and receiver are not collocated, are identical. The following development describes the monostatic geometry (source and receiver may be separated in depth only) since its numerical implementation is somewhat simpler.

Mean reverberation pressure level, *RPL*, can be defined as[5]

$$RPL = SL + DI_T + DI_R + 10\log\left[\frac{\Delta A_b}{R_0^2}\right] - RL_{b,v}, \tag{1}$$

where SL is the source level, DI_T is the directivity index for the transmitter, DI_R is the directivity index for the receiver, ΔA_b is the ensonified area in the horizontal direction, R_0 is the reference distance, and $RL_{b,v}$ is the reverberation loss per unit area for either the bottom interface or the volume, respectively. Where appropriate, these terms have units of decibels relative to 1 μPa and the reference distance of 1 m. At this portion of the theoretical development, reverberation loss per unit area, $RL_{b,v}$, (or simply reverberation

loss) is a full-wave, CW quantity and does not explicitly depend on the angle of interaction. However, because the scattering model is based upon the parabolic approximation in the far-field, a near grazing angle of interaction is still assumed.

1. Bottom Interface Scattering

Reverberation loss per unit area for the bottom interface, RL_b, is defined as[5]

$$RL_b = -20\log\left(\left|p_{2-way,b}\right|\right) - S_b, \tag{2}$$

where $p_{2-way,b}$ is the average normalized, two-way pressure field (based on the long wavelength components of environmental fluctuations) from the transmitter to the scattering patch at the bottom and back to the receiver (to be defined in the next chapter) and S_b is the full-wave scattering strength from small-scale interface roughness. The interface scattering strength, S_b, is defined as[5]

$$S_b = 10\log\left[\frac{k_0^2}{32\pi^2}\left(\frac{\Delta c}{c_0}\right)^2 W_2^{(I)}\left(2k_0\right)\right], \tag{3}$$

where k_0 is the reference wavenumber, Δc is the difference in sound speed between the water and the bottom at the interface, c_0 is the reference sound speed, and $W_2^{(I)}(2k_0)$ is the two-dimensional (2-D) spectrum of the interface roughness evaluated at the Bragg wavenumber for monostatic reverberation. The distinction between long and short wavelength components is chosen to be on the order of a few acoustic wavelengths.

2. Volume Scattering

The nature of the volume reverberation loss is more complex, and it cannot be treated simply in terms of transmission loss adjusted by a scattering term. It can, however, be defined as[5]

$$RL_v = -20\log\left[\int_{\bar{z}_b+\eta_l}^{\infty} p_{2-way,v}(z)\,dz\right] - S_v, \tag{4}$$

where $p_{2-way,v}(z)$ is the normalized two-way pressure field within the volume (to be defined in the next chapter) and S_v is the volume scattering strength. Similar to the interface scattering strength, S_b, the volume scattering strength, S_v, is defined as[5]

$$S_v = 10\log\left[\frac{k_0^2}{32\pi^2} W_{2H}^{(V)}(2k_0)\right]. \tag{5}$$

where $W_{2H}^{(V)}(2k_0)$ is the 2-D horizontal spectrum of the volume fluctuations. This later factor is assumed to be horizontally isotropic and independent of depth when evaluated at the Bragg wavenumber.

It is important to note that all terms other than $RL_{b,v}$ in Eq. (1) are treated as constants. The scattering strengths, $S_{b,v}$, are also assumed to be generally constant over a region of statistically similar perturbations. Therefore, the structure of the mean reverberation pressure level, *RPL,* is dominated by the propagation defined by the two-way normalized pressure, $p_{2-way,(b,v)}$.

B. INTERFACE PERTURBATION

For acoustic scattering from the interface, it has been shown that reverberation loss for the bottom interface, RL_b, is dependent upon the bottom scattering strength, S_b (Eq. (2)). This scattering strength is, in turn, dependent on the two-dimensional (2-D) spectrum of the interface roughness evaluated at the Bragg wavenumber for monostatic reverberation, $W_2^{(I)}(2k_0)$ (Eq. (3)). To further define this 2-D interface roughness, we assume a two-dimensional (2-D) interface spectrum of the form[11]

$$W_2^{(I)}(k_r) = \frac{\mu}{(1+L_{corr}^2 k_r^2)^{\beta/2}}, \tag{6}$$

where k_r is the horizontal spatial wavenumber vector defined by $k_r = \sqrt{K^2 + L^2}$, K and L are the horizontal wavenumbers in the x- and y-directions, respectively, μ is a normalization factor, L_{corr} is a correlation length scale, and β is the spectral exponent. If

this 2-D interface spectrum, $W_2^{(I)}(k_r)$, is also assumed to be isotropic, then the normalization factor, μ, can be defined in terms of the root-mean-square (rms) roughness, σ, such that

$$2\pi\int_0^\infty W_2^{(I)}(k_r)k_r dk_r = \sigma^2, \tag{7}$$

where

$$\mu = \frac{1}{\pi}\left(\frac{\beta}{2}-1\right)\sigma^2 L_{corr}^2. \tag{8}$$

The scattering amplitude can then be determined by evaluating $W_2^{(I)}(k_r)$ at $k_r=2k_0$ since it is the result of Bragg scatter as evaluated along the line of propagation for monostatic reverberation.

To develop an expression for the long-wavelength interface roughness, the one-dimensional (1-D) spectrum along the x-axis is also required. This can be accomplished by taking the 1-D transform of the 2-D interface spectrum, $W_2^{(I)}(K,L)$, along a slice at y=0, which yields

$$W_1^{(I)}(K) = \int_{-\infty}^{\infty} W_2^{(I)}(K,L)dL = \gamma\sigma^2 L_{corr}(1+L_{corr}^2K^2)^{-\frac{\beta}{2}+\frac{1}{2}} \tag{9}$$

where

$$\gamma = \frac{\left(\frac{\beta}{2}-1\right)\Gamma\left(\frac{1}{2}\right)\Gamma\left(\frac{\beta}{2}-\frac{1}{2}\right)}{\pi\Gamma\left(\frac{\beta}{2}\right)}. \tag{10}$$

C. VOLUME PERTURBATION

1. Sound Speed Fluctuations

Similar to acoustic scattering from the bottom interface, reverberation loss due to the bottom volume, RL_v, is dependent upon the volume scattering strength, S_v (Eq. (4)). In turn, the volume scattering strength is dependent on the 2-D horizontal spectrum of the volume fluctuations, $W_{2H}^{(V)}(2k_0)$ (Eq. (5)). To attain this 2-D spectrum, the volume sound

speed perturbations are first modeled by using a three-dimensional (3-D) volume spectrum given by[12]

$$W_3^{(V)}(K,L,M)=\frac{\beta\Lambda^2 B}{2\pi}\left(\Lambda^2\left(K^2+L^2\right)+M^2\right)^{-\frac{\beta}{2}-1}, \tag{11}$$

where B is the spectral strength constant, β is the spectral exponent, $\Lambda=\frac{a_3}{a_1}=\frac{a_3}{a_2}$ is the horizontal-to-vertical aspect ratio used to account for the anisotropy of fluctuations in the sediment, K and L are the horizontal wavenumbers in the x- and y-directions, respectively, and M is the vertical wavenumber.

From this 3-D volume spectrum, we derive a 2-D *horizontal* spectrum through integration yielding

$$W_{2H}^{(V)}(K,L)=\int_{-\infty}^{\infty} W_3^{(V)}(K,L,M)dM\ . \tag{12}$$

Substituting Eq.(11) into Eq.(12), gives us

$$W_{2H}^{(V)}(K,L)=\frac{\beta\Lambda^2 B}{\pi}\int_0^{\infty}\left[\Lambda^2\left(K^2+L^2\right)+M^2\right]^{-\frac{\beta}{2}-1}dM\ . \tag{13}$$

For $\beta=2$, Eq. (13) can be reduced to

$$W_{2H}^{(V)}(K,L)=\frac{\Lambda^2 B}{2}\left[\Lambda^2\left(K^2+L^2\right)\right]^{-\frac{3}{2}}. \tag{14}$$

Also, if the values of $B\sim5\times10^{-4}$ and $\Lambda\sim5$ are chosen as in Yamamoto's work,[12] Eq. (14) can be further reduced to

$$W_{2H}^{(V)}(K,L)=\alpha\left(K^2+L^2\right)^{-\frac{3}{2}}, \tag{15}$$

where

$$\alpha=\frac{B}{2\Lambda}=5\times10^{-5}. \tag{16}$$

For the forward propagation, only the 2-D *vertical* spectrum in the (x,z) plane is required. It can be similarly defined by reducing the spectrum according to

$$W_{2V}^{(V)}(K,M)=\int_{-\infty}^{\infty}W_3^{(V)}(K,L,M)dL=\frac{\beta\Lambda^2 B}{2\pi}\int_{-\infty}^{\infty}\left[\Lambda^2\left(K^2+L^2\right)+M^2\right]^{-\frac{(\beta+2)}{2}}dL. \quad (17)$$

For $\beta=2$, Eq. (17) reduces to

$$W_{2V}^{(V)}(K,M)=\alpha'\left[25K^2+M^2\right]^{-\frac{3}{2}}, \quad (18)$$

where $\alpha'=1.25\times10^{-3}$.

2. Density Fluctuations

Many of the inhomogeneities within the bottom volume that result in reverberation are caused by variations in the bottom volume density, ρ. The effect of these variations in density is treated though the definition of the effective index of refraction,[8]

$$n'^2=n^2+\frac{1}{2k_0^2}\left[\frac{1}{\rho}\nabla^2\rho-\frac{3}{2}\left(\frac{1}{\rho}\nabla\rho\right)^2\right]. \quad (19)$$

By assuming that the environment is approximately range-independent for any particular scattering patch and that sediment properties are nearly horizontally stratified, we may simplify this expression for the effective index of refraction to

$$n'^2=n^2+\frac{1}{2k_0^2}\left[\frac{1}{\rho}\frac{\partial^2\rho}{\partial z^2}-\frac{3}{2}\left(\frac{1}{\rho}\frac{\partial\rho}{\partial z}\right)^2\right]. \quad (20)$$

For forward propagation, the sound speed index of refraction is based only on large scale features, such that

$$n_b^2\rightarrow\hat{n}_b^2\left(\vec{r},z\right)=\frac{c_0^2}{\overline{c}_b^2}. \quad (21)$$

$\overline{c}_b$ is defined as

$$\overline{c}_b=c_{b_0}\left(1+b_z+\delta_l\right)=c_{b_0}+\delta c_b\ , \quad (22)$$

where c_{b_0} is the mean bottom sound speed at the interface, b_z is the normalized gradient of bottom sound speed defined by $b_z = g/c_{b_0}$, δ_l is the zero-mean random perturbation for the long wavelength component, and $\delta c_b = c_{b_0}\left(b_z + \delta_l\right)$,.

Yamamoto's analysis [12] states that the relative fluctuations in density relate to the relative fluctuations in sound speed according to the relationship

$$\frac{\delta\rho}{\rho_0} = \frac{2\left(\rho_r - \rho_0\right)}{2\rho_0 - \rho_r}\frac{\delta c}{c_0} = 2\gamma\frac{\delta c}{c_0}, \tag{23}$$

where

$$c_0 = c_{b_0}\left(1 + b_z\right) \text{ and } \gamma = \frac{\rho_r - \rho_0}{2\rho_0 - \rho_r}\ . \tag{24}$$

In this case, ρ_0 and c_0 are the ambient values of the density and sound speed in the sediment, respectively, and ρ_r is the density of the grain (chosen as $2650\,kg/m^3$). This allows us to express the bottom volume density as

$$\rho = \rho_0 + \delta\rho = \rho_0\left[1 + \frac{2\gamma}{c_0}\delta c\right]. \tag{25}$$

Taking the first and second partial derivatives of Eq. (25) with respect to depth, z, and neglecting depth gradients in either c_0 or ρ_0, we obtain expressions for both the change in density and rate of change in density with depth

$$\frac{\partial\rho}{\partial z} = \frac{2\gamma\rho_0}{c_0}\frac{\partial}{\partial z}\left(\delta c\right) \tag{26}$$

and

$$\frac{\partial^2\rho}{\partial z^2} = \frac{2\gamma\rho_0}{c_0}\frac{\partial^2}{\partial z^2}\left(\delta c\right). \tag{27}$$

D. TURBULENT SOUND SPEED PERTURBATION

Understanding the mechanism of reverberation from the elements of the bottom is an important step in predicting the expected reverberation from the sea floor. However,

these acoustic signals must still travel through the water column on their way from source to bottom scattering patch and from the scattering patch to the receiver. Small-scale fluctuations in sound speed within the water column can alter the paths of travel for these acoustic signals on their way to and from each scattering patch and therefore affect the overall structure of the reverberation. Such fluctuations are common and are often the result of oceanic phenomena such as turbulence or internal waves.[17]

Of the phenomena that generate water volume sound speed fluctuations, we will place our emphasis on the effect of turbulence since the focus of our later analysis will be on reverberation signal coherence. To characterize the turbulent perturbation field, a statistical model is used. In this method, the turbulent field is approximated as a random realization of perturbations based on an accepted power spectral density of the turbulence. This approach should be consistent with perturbation theory[14], which is only valid for the weak scattering regime, the case where the induced change in the signal strength is not large enough to exceed the average signal strength.[17]

The index of refraction for perturbations, $\mu(\vec{r})$, is defined as

$$\delta n(\vec{r}) = \frac{\delta c(\vec{r})}{c(\vec{r})} \equiv \mu(\vec{r}), \tag{28}$$

where $\delta c(\vec{r})$ is the change in sound speed and $c(\vec{r})$ is the sound speed along the path. In this case, the variance of $\mu(\vec{r})$ can be written as

$$\mathrm{var}(\mu(\vec{r})) = \frac{1}{(2\pi)^3} \int_{-\infty}^{\infty} S_\mu(\vec{k}) d^3k, \tag{29}$$

where $S_\mu(\vec{k})$ is the spectral density of the perturbations in units of m^3 and the integral is calculated over the entirety of three dimensional (3-D) wavenumber space, $\vec{k} = (K, L, M)$. Because the perturbation region is not bounded, the variance is normalized according to

$$\mathrm{var}(\mu(\vec{r})) = \left\langle \left| \mu(\vec{r}) \right|^2 \right\rangle = \frac{1}{volume} \int_V \mu^2(\vec{r}) d^3r \tag{30}$$

Combining Eqs. (29) and (30) yields the relationship

$$\int_V \mu^2(\vec{r})d^3r = \frac{volume}{(2\pi)^3}\int_{-\infty}^{\infty} S_\mu(\vec{k})d^3k\,. \tag{31}$$

The transform of the index of refraction, $\mu(\vec{r})$, to the signal spectrum, $F_\mu(\vec{k})$, can now be defined as

$$\mu(\vec{r}) = \frac{1}{(2\pi)^3}\int_{-\infty}^{\infty} F_\mu(\vec{k})e^{i\vec{k}*\vec{r}}d^3k\,. \tag{32}$$

Using this transform, the correlation of $\mu(\vec{r})$ can be written as

$$\int_{-\infty}^{\infty}\mu(\vec{r})\mu^*(\vec{r}-\vec{r}')d^3r = \frac{1}{(2\pi)^6}\int_{-\infty}^{\infty} d^3r\left[\int_{-\infty}^{\infty} F_\mu(\vec{k})e^{i\vec{k}*\vec{r}}d^3k\right]\left[\int_{-\infty}^{\infty} F_\mu^*(\vec{k}')e^{-i\vec{k}*(\vec{r}-\vec{r}')}d^3k\right] \tag{33}$$

where $\left|F_\mu(\vec{k})\right|^2$ is the Fourier transform of the correlation function. The interrelation between the square of the signal spectra, $F_\mu(\vec{k})$, and the spectral density, $S_\mu(\vec{k})$, can be determined by setting $\vec{r}'$ to zero to yield

$$\left|F_\mu(\vec{k})\right|^2 = (volume)*S_\mu(\vec{k})\,, \tag{34}$$

which can be rewritten as

$$\left|F_\mu(\vec{k})\right| = \left[volume*S_\mu(\vec{k})\right]^{1/2}. \tag{35}$$

A similar process holds in 2-D. Holding one of the variables at a fixed value can create a planar slice. Holding *y* constant at *y=0* yields

$$\frac{1}{Area}\iint_A \mu^2(x,0,z)dxdz = \frac{1}{(2\pi)^2}\int_{-\infty}^{\infty}\int_{-\infty}^{\infty} V_\mu(K,M)dKdM\,, \tag{36}$$

where $V_\mu(K,M)$ is the two-dimensional (2-D) spectral density along the plane *y* = 0. Furthermore, we can also represent the index of refraction as

$$\mu(x,z) = \frac{1}{(2\pi)^2}\int_{-\infty}^{\infty}\int_{-\infty}^{\infty} G_\mu(K,M)e^{i(Kx+Mz)}dKdM\,, \tag{37}$$

where $G_\mu(K,M)$ is the spectral transform of the 2-D perturbation field. The forms of Eq. (36) and (37) suggest a relation similar to (35),

$$\left|G_\mu(K,M)\right| = \left[\, Area * V_\mu(K,M) \right]^{1/2}. \tag{38}$$

The 2-D spectral density, $V_\mu(K,M)$, can also be derived from the 3-D spectral density, $S_\mu(\vec{k})$, as [14]

$$V_\mu(K,M) = \frac{1}{2\pi} \int_{-\infty}^{\infty} S_\mu(K,L,M)\,dL\,. \tag{39}$$

Now that we have developed expressions to relate sound speed fluctuations to spectral densities, we must leverage these relationships to produce the turbulent perturbation field. This field can be approximated through the use of the method of structure functions.[14] This method uses both isotropic and homogeneous approximations. It also reduces the scale of the analysis; therefore large-scale perturbations are not accounted for. Using standard statistical relations, the 3-D spectral density function can be written in the form [17]

$$E(k) = A\varepsilon^{2/3}k^{-11/3}, \tag{40}$$

where $E(k)$ is the spectral density, A is a scalar multiplier, ε is the energy dissipation rate, and $k^2 = K^2 + L^2 + M^2$. A lower wavenumber threshold limit, k_t, is also established such that the $K^{-11/3}$ dependence becomes

$$E(k) \approx \frac{1}{(k^2 + k_t^2)^{11/6}}\,. \tag{41}$$

This prevents $E(k)$ from blowing up at small values of k. A highpass filter of the form

$$\frac{k^2}{k^2 + k_t^2} \tag{42}$$

is also applied to force $E(k)$=0 when k=0. A high-frequency cut-off based on the Batchelor spectrum is then introduced defined by [17]

$$R_B(k) = \exp\left[-q\left(\frac{k}{k_B}\right)^2\right], \tag{43}$$

where q is an order unity factor (in this case, a value of 3.7 will be used to maintain consistency with previous work),[17] and k_B is the Batchelor wavenumber. This Batchelor wavenumber can, in turn, be expressed as

$$k_B = \left(\frac{\bar{\varepsilon}}{\nu\kappa_T^2}\right)^{1/4}, \tag{44}$$

where $\bar{\varepsilon}$ is the depth averaged kinetic energy dissipation rate in units of W/kg, v is the kinematic viscosity (1.40e-6 m^2/s), and κ_T is the thermal diffusivity of sea water (≈1.00e-7 m^2/s).

An expression for the depth averaged kinetic energy dissipation rate has been developed for the turbulence caused by the decay of internal waves. This expression was originally developed for use in deep-water problems and its applicability to shallow water remains unknown. In this development, the depth averaged kinetic energy dissipation rate, $\bar{\varepsilon}$, is defined as [15]

$$\bar{\varepsilon} = 0.3\frac{1}{f_I}\left\langle\left[\frac{4}{\pi} j_* N(z) b\mathrm{E}_{GM} f_I\right]^2 \cosh^{-1}\left(\frac{N(z)}{f_I}\right)\right\rangle_Z, \tag{45}$$

where f_I is the inertial frequency in units of rad/sec, j_* is the mode number ($j_* = 1$ is the characteristic mode for shallow water), *N(z)* is the buoyancy frequency in rad/sec, and $b\mathrm{E}_{GM}$ is a measure of internal wave intensity ($\cong 0.5m$). The notation $\langle\ \rangle_Z$ denotes a depth average. The buoyancy frequency, *N(z)*, can be computed using

$$N(z) = g^{1/2}\left[\frac{1}{\rho(z)}\frac{\partial\rho_p(z)}{\partial z}\right]^{1/2}, \tag{46}$$

where $\rho(z)$ and $\rho_p(z)$ are the density and the potential density as a functions of depth, respectively.

Following this development, the 3-D spectral density can now be written in the form

$$S_\mu(k;z) = \frac{A_\mu(z)}{(k^2+k_t^2)^{11/6}} \frac{k^2}{k^2+k_t^2} R_B(k) . \tag{47}$$

where $A_\mu(z)$ is introduced as the turbulent strength parameter in units of $m^{-2/3}$.[15] This parameter is defined as

$$A_\mu(z) = 2.6a^2\Gamma_m \left(\frac{4}{\pi} j_* N(z) b \mathrm{E}_{GM}\right)^{4/3} \left\langle \left(\frac{\partial T'}{\partial z}\right)^2 \right\rangle \left(\frac{\ln\left(2N(z)/f_I\right)}{\left(2N(z)/f_I\right)}\right)^{2/3}, \tag{48}$$

where a = 3.2e-3(°C)$^{-1}$, $\Gamma_m = 0.2$, and $\left\langle \left(\frac{\partial T'}{\partial z}\right)^2 \right\rangle$ is the variance of the temperature gradient. This parameter varies slowly with respect to the correlation length scales of the turbulence, so the previous isotropic assumption holds locally.

To develop a 2-D spectral density, integration can be applied to the portion that varies with the turbulent spectrum only. The remaining terms such as the turbulent strength parameter and wavenumber roll-off can then be included afterwards. The portion of spectral density that varies with the turbulent spectrum only can be written as

$$\Phi_{3D}(k) = \frac{1}{(k^2+k_t^2)^{11/6}} . \tag{49}$$

The 2-D spectral density is derived through integration as

$$\Phi_{2D}(K,M) = \frac{1}{2\pi} \int_{-\infty}^{\infty} \Phi_{3D}(K,L,M) dL$$

$$= \frac{1}{2\pi} \int_{-\infty}^{\infty} \frac{1}{(K^2+L^2+M^2+k_t^2)^{11/6}} dL . \tag{50}$$

Substituting $\alpha^2 = K^2 + M^2 + k_t^2$ into Eq. (50) yields

$$\Phi_{2D}(K,M) = \frac{1}{\pi\alpha^{11/3}} \int_0^\infty \frac{1}{\left(1 + L^2/\alpha^2\right)^{11/6}} dL \,. \tag{51}$$

Solving this integral (from an integral table) produces the expression

$$\Phi_{2D}(K,M) = \frac{1}{2\pi\alpha^{8/3}} \frac{\sqrt{\pi}\Gamma(\frac{4}{3})}{\Gamma(\frac{11}{6})} \,. \tag{52}$$

When the terms that do not vary with the turbulent spectrum are reapplied, the resulting expression for 2-D spectral density of turbulent fluctuations becomes

$$V_\mu(k;z) = \frac{\sqrt{\pi}}{2\pi} \frac{\Gamma\left(\frac{4}{3}\right)}{\Gamma\left(\frac{11}{6}\right)} \frac{A_\mu(z)}{(k^2 + k_t^2)^{4/3}} \frac{k^2}{k^2 + k_t^2} R_B(k) \,. \tag{53}$$

E. CORRELATION METHOD OF SEPARATING AND DISCRIMINATING VOLUME AND SURFACE SCATTERING

In the shallow water environment, the primary contributors to reverberation are the roughness of the bottom interfaces and the inhomogenieties within the bottom volume. A reverberant return in this type of environment is essentially the combined effect of these two factors. In some cases, it would be desirable to have a metric for the degree to which each factor contributes to the total reverberation. For example, methods for determining the bottom sediment type and extracting certain bottom parameters from the reverberant return have been proposed.[13] However, these methods require that the primary contributor to the reverberation be known. The influence of changes in source and environmental parameters on the reverberation contributions from both the interfaces and the bottom would be useful as well.

To separate the contributions of the interface roughness and volume perturbation components, the following approach is suggested based on the work of Ivakin.[13] This approach involves the measurement of the spatial coherence of the reverberant field. If the two contributors are uncorrelated with respect to each other, then the contribution from interface roughness, p_r, and the contribution from bottom volume perturbations, p_v, have intensities, I_r and I_v respectively, that are additive as

$$I = \left\langle |p|^2 \right\rangle = I_r + I_v , \tag{54}$$

where I is the total intensity and $p = p_r + p_v$, the coherent sum of the two reverberation pressure signals. The spatial coherence coefficient, N, can then be defined as

$$N(r_1, r_2) = \frac{\langle p(r_1) p^*(r_2) \rangle}{\sqrt{I(r_1) I(r_2)}} , \tag{55}$$

where r_1 and r_2 are the spatial positions of two receiving elements. Once the distance between the receiving elements and the scattering patch, R, becomes sufficient such that $L = |r_1 + r_r| \ll R$, the resulting spatial coherence coefficient becomes

$$N(L) = \frac{I_r}{I} N_r(L) + \frac{I_v}{I} N_v(L) . \tag{56}$$

If these partial roughness and volume coherence coefficients, N_r and N_v for the interface roughness and bottom volume perturbations, respectively, have significantly different coherence scales, then the contribution of each component can be determined through measurements of the spatial coherence of the reverberant field.

Consider the case of a near backscattering geometry in which the bottom volume has the same sound speed as the water and the attenuation coefficient $\beta = 2k\delta$ where δ is the loss parameter for a particular bottom type. The expression for the partial roughness coherence coefficient can be obtained [13] as

$$N_r(L) = e^{ikL\sin\chi} \frac{\sin(L/L_r)}{(L/L_r)} , \tag{57}$$

where χ is the grazing angle and $L_r = \frac{2H(T/\tau)}{\pi \sin^2 \chi}$ for a period, T, and a duration, τ. This approximation holds for the case when $\tau/2 \ll R/c$. A similar expression is available for the partial volume coherence coefficient in the form of

$$N_v(L) = e^{ikL\sin\chi} \frac{1}{1 - i(L/L_v)} , \tag{58}$$

where $L_v = \frac{4H\delta}{\sin^2 \chi}$. This approximation holds for the case when $1/\beta \ll R$.

For this case, the expression for the partial roughness coherence coefficient, N_r, displays a dependence on the signal duration, τ, while the expression for partial volume coherence coefficient, N_v, displays a dependence on the sediment parameters by way of the loss parameter, δ. The different effects of the two partial coherence coefficients can be more easily seen if parameters are chosen. The cases where H=30m, χ=60°, δ=0.005 (which corresponds to the loss parameter for silt), and signal durations, τ, of 10T and 5T developed in Ivakin's work [13] are shown in Figure 1. In this figure, the different natures of the partial roughness coherence coefficients are clearly visible.

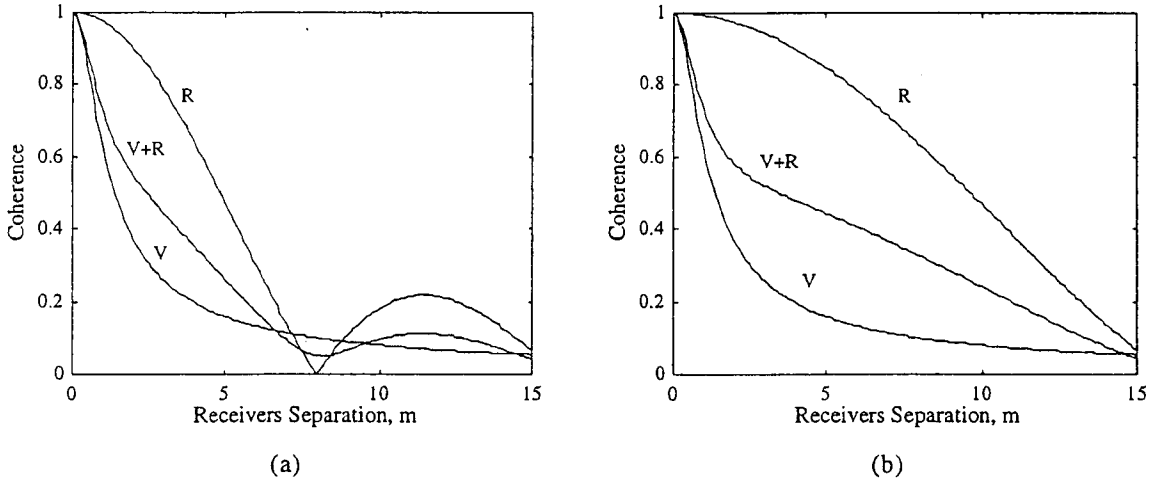

Figure 1. Coherence Coefficient Magnitude Plots for Two Pulse Durations, (a) τ=10T and (b) τ=5T (from [13])

This method describes an interesting and potentially powerful analysis tool. It also suggests a similar frequency-domain analog for broadband signals. In the previous example, pulse lengths are chosen with respect to period such that τ/T is held constant at values of 10 and 5, respectively. This is analogous to holding the ratio between center frequency, *fc*, and bandwidth, *BW*, fixed at the *same* constant such that $\tau/T = fc/BW$. As such, similar differences in spatial coherence should be produced by employing different bandwidths, produced either by varying the source spectrum or band-pass filtering of the received broadband signal. Given an accurate model to predict the

expected spatial coherence for a given environment and geometry, spatial coherence analysis of broadband data analyzed at different bandwidths produces consistent results as the narrow-band, pulse length varied theory indicates.[19]

III. NUMERICAL METHODS

A. MONTEREY-MIAMI PARABOLIC EQUATION (MMPE) MODEL

As the name suggests, the MMPE Model[8] is based on the parabolic approximation to the acoustic wave equation. This approach begins by first representing the time harmonic acoustic field in cylindrical coordinates. Azimuthal symmetry is then assumed since ocean environments tend to display weak azimuthal dependence. The resulting acoustic field can then be represented as

$$P\left(r,z,\omega t\right)=p\left(r,z\right)e^{-i\omega t}. \tag{59}$$

Substituting Eq. (59) into the wave equation in cylindrical coordinates yields the Helmholtz equation,

$$\nabla^2 p(r,z)+\frac{\omega^2}{c(r,z)^2}p(r,z)=0, \tag{60}$$

where

$$\nabla^2=\frac{1}{r}\frac{\partial}{\partial r}r\frac{\partial}{\partial r}+\frac{\partial^2}{\partial z^2}. \tag{61}$$

The Helmholtz equation can then be factored by introducing an operator, Q_{op}, with the notation

$$Q_{op}=(\mu+\varepsilon+1)^{\frac{1}{2}}, \tag{62}$$

where

$$\mu=\frac{1}{k_o^2}\frac{\partial^2}{\partial z^2},\ \varepsilon=n^2-1, \tag{63}$$

and the index of refraction $n=\frac{c_0}{c}$, where c_0 is the reference sound speed of the ocean volume.

Once the effect of cylindrical spreading is considered and the Helmholtz equation is properly factored, the out-going acoustic pressure can then be defined as [9],

$$p(r,z) = P_o \sqrt{\frac{R_o}{r}} Q_{op}^{-1/2} \psi(r,z) e^{ik_o r}, \tag{64}$$

where $\psi(r,z)$ is the envelope function or PE field function and P_o is the pressure amplitude at R_o. The parabolic equation for the PE field function, $\psi(r,z)$, is then defined by

$$\frac{\partial \psi}{\partial r} = -ik_o \psi + ik_o Q_{op} \psi = -ik_o H_{op} \psi, \tag{65}$$

where H_{op} is a Hamiltonian-like operator defined by

$$H_{op} = 1 - Q_{op}, \tag{66}$$

which defines the evolution of the PE field function in range. The relationship between values of ψ at different ranges can be defined by

$$\psi(r + \Delta r) = \Phi(r) \psi(r), \tag{67}$$

where $\Phi(r)$ is a propagator that accounts for the change in the values of ψ with range. A split-step Fourier (PE/SSF) method[10] can then be used to determine this propagator, $\Phi(r)$. The Fast Fourier Transform (FFT) allows the PE/SSF implementation to be represented by[8]

$$\psi(r + \Delta r, z) = e^{-ik_o \frac{\Delta r}{2} U_{op}(r+\Delta r, z)} FFT \left\{ e^{-ik_o \Delta r \hat{T}_{op}(k_z)} IFFT \left(e^{-ik_o \frac{\Delta r}{2} U_{op}(r,z)} \psi(r,z) \right) \right\} \tag{68}$$

where

$$U_{op} = -[n - 1] \tag{69}$$

and

$$\hat{T}_{op} = 1 - \left[1 - \left(\frac{k_z}{k_o} \right)^2 \right]^{1/2}. \tag{70}$$

B. NUMERICAL IMPLEMENTATION

At this point, we've described the applicable concepts of reverberation theory, particularly the effects of scatter from bottom interfaces and the bottom volume in terms of reverberation loss. We've also described methods for generating perturbations in the interface roughness, the bottom volume, and the turbulent sound speed in the water column. The next step is to apply all of this theory in such a manner as to produce useful results from numerical analysis. The following describes the application of this theory to the MMPE Model.

1. Interface Roughness

In the discussion of interface perturbation theory, the 1-D interface spectrum was developed (Eq.(9)). In order to generate a 1-D roughness realization from this 1-D spectrum, we define the roughness realization as

$$\eta(x) = \int_{-\infty}^{\infty} S_1(K) e^{iKx} dK \,, \tag{71}$$

where

$$S_1(K) = \left[W_1^{(I)}(K) \right]^{1/2} A(K) e^{i\theta(K)} \,. \tag{72}$$

$A(K)$ provides a random amplitude and $\theta(K)$ provides a random phase. Combined, these components form a randomization factor of the form, $Ae^{i\theta}$, for which the complex amplitude exhibits a normal distribution. To accomplish this, the phase component is a random variable that is distributed uniformly over the interval $[0, 2\pi]$. In practice, this component is generated by

$$\theta = 2\pi r_1 \,, \tag{73}$$

where r_1 is a uniformly distributed random variable over the interval [0,1]. The amplitude component is a random variable with a Rayleigh distribution generated by

$$A = \sqrt{-\ln(r_2)} \,, \tag{74}$$

where r_2 is another uniformly distributed random variable over the interval [0,1]. When applied to the MMPE model, the actual relationship used is

$$W_1^{(I)}(K) = \left(1 + L_{corr}^2 K^2\right)^{-\frac{\beta}{2}+\frac{1}{2}} \tag{75}$$

and the final result is normalized, i.e. $\dfrac{\eta(x)}{\left\langle \eta^2(x) \right\rangle^{\frac{1}{2}}}$. The actual rms perturbation is then achieved by simply multiplying the result by the desired rms value.

2. Bottom Volume Sound Speed Perturbations

In the discussion of bottom volume perturbation theory, the 2-D vertical spectrum was developed (Eq. (17) and (18)). In a fashion similar to that used for 1-D interface roughness realizations, a 2-D vertical volume sound speed fluctuation realization is defined as

$$c_0 \delta(x,z) = \int_{-\infty}^{\infty} \int_{-\infty}^{\infty} S_2(K,M) e^{iKx} e^{iMz} dK dM \ , \tag{76}$$

where

$$S_2(K,M) = \left[W_{2V}^{(V)}(K,M) \right]^{1/2} A(K,M) e^{i\theta(K,M)} \ . \tag{77}$$

Both $A(K,M)$ and $\theta(K,M)$ are similar to the random values $A(K)$ and $\theta(K)$ introduced in Eq. (72). Specifically, they are generated by

$$\theta(K,M) = 2\pi r_1(K,M) \tag{78}$$

and

$$A(K,M) = \sqrt{-\ln(r_2(K,M))} \ , \tag{79}$$

respectively, where both $r_1(K,M)$ and $r_2(K,M)$ are now a matrix of uniformly distributed random numbers in [0,1]. When applied to the MMPE model, the actual relationship used is

$$W_{2V}^{(V)}(K,M) \propto \left(\Lambda^2 K^2 + M^2\right)^{-\frac{\beta}{2}-1} \ , \tag{80}$$

and the result is normalized and rescaled by the desired rms values.

3. Bottom Volume Density Fluctuations

The definition for 2-D vertical volume sound speed fluctuation realizations (Eq. (76)) can also be combined with the results from density fluctuation theory (Eqs. (26) and (27)) to provide a realization for the bottom density fluctuations as well. Specifically, substituting Eq. (76) into Eqs. (26) and (27) yields both

$$\frac{\partial \rho}{\partial z} = \frac{2\gamma p_0}{c_0} \int_{-\infty}^{\infty} \int_{-\infty}^{\infty} (iM) S_2(K,M) e^{iKx} e^{iMz} dK dM \tag{81}$$

and

$$\frac{\partial^2 \rho}{\partial z^2} = \frac{2\gamma p_0}{c_0} \int_{-\infty}^{\infty} \int_{-\infty}^{\infty} (-M^2) S_2(K,M) e^{iKx} e^{iMz} dK dM \,. \tag{82}$$

The sediment effective index of refraction is then derived by substituting Eq. (81) and Eq. (82) into the expression for the effective index of refraction, n'^2, Eq. (20), yielding

$$n_b'^2(x,z) = n_b^2(x,z) + \frac{1}{2k_0^2}\left[\alpha(x,z) + \beta(x,z)\right], \tag{83}$$

where

$$\alpha(x,z) = \frac{-2\gamma}{c_0(x,z)} \iint M^2 S_2(K,M) e^{iKx} e^{iMz} dK dM \tag{84}$$

and

$$\beta(x,z) = +\frac{3}{2}\left[\frac{2\gamma}{c_0(x,z)} \iint M S_2(K,M) e^{iKx} e^{iMz} dK dM\right]^2 . \tag{85}$$

Both of these parameters are computed in parallel with δc_b during the implementation of the MMPE model. An additional propagator term is then used in the sediment

$$\Phi_\rho(x,z) = e^{i\Delta r k_0 U_\rho(x,z)}, \tag{86}$$

where

$$U_\rho(x,z) = -\frac{1}{4k_0^2}\left[\alpha(x,z) + \beta(x,z)\right]. \tag{87}$$

4. Water Volume Sound Speed Turbulence

The relationship between the 2-D spectral density of turbulent fluctuations, $V_\mu(k;z)$, and the 2-D index of refraction for perturbations, $\mu(x,z)$, (also known as the perturbation field) is evident in Eqs. (37) and (38). Using this relationship, random realizations of $\mu(x,z)$ are generated by modifying Eq. (37) to create the expression

$$\mu(x,z) = \frac{1}{(2\pi)^2} \int_{-\infty}^{\infty} \int_{-\infty}^{\infty} \left[G_\mu(K,M_z) A(K,M) e^{i\theta(K,M)} \right] e^{i(Kx+Mz)} dK dM \,, \tag{88}$$

where $A(K,M)$ provides a 2-D random amplitude for each wavenumber component and $\theta(K,M)$ provides a 2-D random phase component similar to the random values $A(K,M)$ and $\theta(K,M)$ introduced in Eqs. (79) and (80).

The 2-D sound speed perturbation field is then easily obtained from this realization of the perturbation field by multiplying by c_o, since $\delta c(x,z) = c_o \mu(x,z)$. At this point, randomizations in the perturbation field have been generated, but no regard has been given to scale. As before, after the realization of the perturbation field is created, the result is simply normalized and rescaled by the desired rms value.

C. TIME-DOMAIN PROCESSING

The preceding development has covered reverberation loss theory and developed a method for its numerical implementation. This development is based on continuous wave (CW) analysis, which holds for discrete frequencies. However, to obtain the structure of the multipath pulse propagation in time, broadband analysis is required. To create a broadband source, the MMPE model is run for a large number of discrete frequencies to generate an output over a given frequency band. Time domain analysis then extracts the nature of the two-way travel time structure of the reverberation loss from both the interface and the volume reverberation. The reverberant field at each range step can then be determined and the propagation continued through the water column.

1. Time-Domain Analysis of Interface

The basic geometry of a typical two-way return from a scattering patch as adapted from Smith and Cushman[4] is depicted in Figure 2. The travel time structure of the one-way forward propagating field at a given range step r_m is denoted as $p_+(r_m,z,t)$, where t is

the reduced time defined as $t = T - \frac{r_m}{c_0}$, and T is the actual travel time. The two-way pressure field as observed at the receiving element is determined by performing the convolution of two, one-way propagated fields in the time-domain[4]

$$p_{2-way,b}(r_m,\tau) = \int p_{+Tb}(r_m,t)\,p_{+Rb}(r_m,\tau-t)\,dt\,, \tag{89}$$

where $p_{+Tb}(r_m,t)$ and $p_{+Rb}(r_m,\tau-t)$ are the forward propagated pressure fields from the transmitter and receiver to the scattering point as evaluated at the bottom interface for the range step r_m, respectively, and τ is the reduced time of the reverberation defined as $\tau = T - \frac{2r_m}{c_0}$. Reciprocity allows the forward propagating pressure field from receiver to scattering patch, p_{+Rb}, to replace the return path, p_{-Rb}, since these two propagated fields are identical.

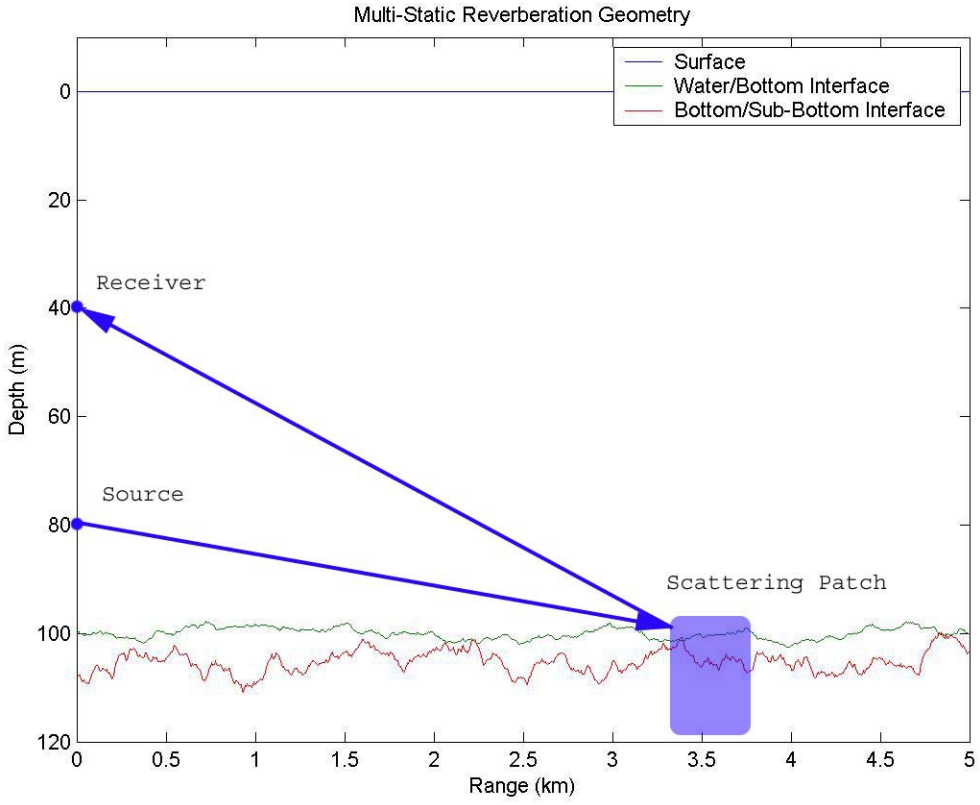

Figure 2. Bistatic Return From Scattering Patch

In practice, this time-domain convolution of the two pressure fields can be more easily calculated in the frequency domain, where the operator becomes a scalar multiplication of the two functions. This allows the two-way field from the interface to be expressed in the frequency domain as

$$p_{2-way,b}(r_m, f) = p_{+Tb}(r_m, f)\, p_{+Rb}(r_m, f), \tag{90}$$

where

$$p_{+Tb}(r_m, f) = \frac{1}{\sqrt{r_m}} \psi_{+Tb}(r_m, f) e^{ik_0 r} \tag{91}$$

and

$$p_{+Rb}(r_m, f) = \frac{1}{\sqrt{r_m}} \psi_{+Rb}(r_m, f) e^{ik_0 r} \ . \tag{92}$$

For each bottom scattering patch, the two-way travel time structure of the reverberation loss for the bottom interface, RL_b, can then be defined as

$$p_{-b}(r_m, t) = A \int p_{2-way,b}(r_m, f) e^{-i2\pi ft} df \ , \tag{93}$$

where the constant A is included to incorporate all the other factors needed to define reverberation loss, RL_b. This provides the two-way travel time structure due to scattering from a single range step, r_m. This calculation is then conducted for each range step, and the total field at the receiver is computed as the coherent sum of the pressure values from all of the range steps, r_m. This is accomplished by matching up the discrete arrival times, t_n, according to the relation

$$p_{-b}(t_n) = \sum_{m=1}^{M} p_{-b}(r_m, t_n), \tag{94}$$

where p_{-b} is the total interface reverberation pressure received at the receiver at time t_n.

2. Time-Domain Analysis of Volume

The time domain analysis is more complicated for the bottom volume since multiple depth steps must also be taken into account. In a manner similar to that used for the interface analysis (Eq. (90)), the reverberant field due to each point in range and depth is computed by combining the source-to-patch and the patch-to-receiver propagating field in the frequency domain using

$$p_{2-way,v}(r_m, z, f) = n(r_m, z)\, p_{+T}(r_m, z, f)\, p_{+R}(r_m, z, f)\,, \tag{95}$$

where r_m is the range step, z is the depth step ($z > z_b$ for the bottom volume), f is the frequency, and $n(r_m, z)$ is the local index of refraction. A Fourier transform yields the appropriate time-domain response

$$p_{2-way,v}(r_m, z, t) = B \int p_{2-way,v}(r_m, z, f) e^{-i2\pi ft} df\,, \tag{96}$$

where B is a constant that accounts for all the other terms needed to define the reverberation loss, RL_v. The two-way travel time structure of the reverberation loss for the volume, RL_v, can then be derived from

$$p_{-v}(r_m, t) = \int_{z>z_b}^{\infty} p_{2-way,v}(r_m, z, t) dz\,, \tag{97}$$

which is the coherent sum over all depths below the interface at a range step m. Each single set of time series can then be matched and summed as

$$p_{-v}(t_n) = \sum_{m=1}^{M} p_{-v}(r_m, t_n)\,, \tag{98}$$

where p_{-v} is the two-way time domain pressure defining the volume reverberation loss as measured at the receiver at time t_n due to the entire bottom volume.

D. MODELING PARAMETERS

1. Numerical Analysis Geometry

The use of a vertical linear array (VLA) during ASIAEX allowed for the capture of varying spatial properties in the acoustic return along its axis. The utility of analyzing such spatial variation has been shown through a discussion of the correlation method of separating and discriminating volume and surface scattering.[13] However, this method requires an accurate prediction of the expected spatial response of the interfaces and the bottom volume for a given geometry. It is therefore desirable to generate a similar vertical array for the numerical analysis to produce the required prediction. In this case, a 16-element array was modeled. This modeled VLA extends 60m, from 20m to 80m in depth, with a constant 4m vertical separation between elements as shown in Figure 3.

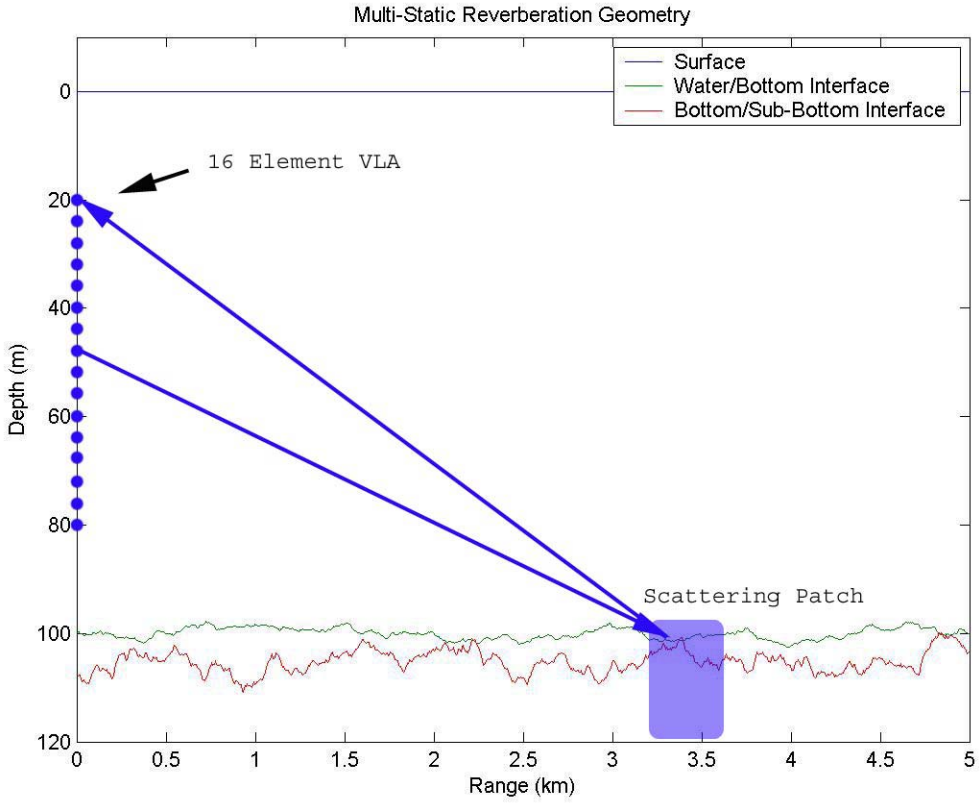

Figure 3. Geometry of VLA and Scattering Patch

The problem geometry and environmental parameters are chosen to closely simulate the conditions observed during the ASIAEX. This modeled environment includes both a water/bottom interface at an average depth of 100m and a bottom/sub-bottom interface at an average depth of 105m - to simulate both the smoother, softer and more penetrable bottom layer of sand and mud - and a harder sub-bottom layer of coarser sand, gravel or rocks. The element at 48m is chosen as the source, since it is close to the set charge depth of 50m. The sound speed profile (SSP) was taken directly from CTD measurements taken during the ASIAEX, averaged over the duration of the exercise. The choice of frequency bands and the geometry of the vertical array geometry are made to approximate ASIAEX as close as possible while still allowing for reasonable calculation speeds. The maximum propagation range is 5km to capture most of the environmental contributors to the reverberation loss.

To ensure that the results of the numerical analysis hold for a variety of environmental parameters, the numerical analysis was also conducted for a number of environmental variations. In each case, only one parameter was varied from the "reference." The parameters for this reference environment are a 1m rms variation in the water/bottom interface roughness, a 2m rms variation in the bottom/sub-bottom interface roughness, a 15 m/s rms bottom volume sound speed perturbation, and no water volume sound speed turbulence. All comparisons of environmental parameters are done with respect to a single realization of this reference model.

2. The Modeled Environment and Variations

a. Variations in Interface Roughness

Three variations in bottom interface roughness were generated. In addition to the reference condition of 1m water/bottom interface roughness and 2m rms bottom/sub-bottom interface roughness, a lower roughness realization of 0.5m and 1m rms and a higher roughness realization of 2m and 4m rms water/bottom and bottom/sub-bottom interface roughness, respectively, were calculated and analyzed. Graphical representations of all three realizations are depicted in Figure 4.

b. Bottom Volume Sound Speed Perturbations

To model an environment with a soft bottom and a harder sub-bottom, the sound speed of the bottom layer was set at 1700m/s while the sound speed of the sub-bottom layer was set at 1760m/s. Three variations in bottom volume sound speed perturbations were also generated. In addition to the reference condition of a 15m/s rms bottom volume sound speed perturbation, a lesser perturbation realization of 5m/s rms and a greater perturbation realization of 45m/s rms bottom volume sound speed perturbation were calculated and analyzed. This greater perturbation realization is somewhat more dramatic than what is expected to occur naturally, but it is still useful as a means of comparison. Graphical representations of all three realizations are depicted in Figure 5.

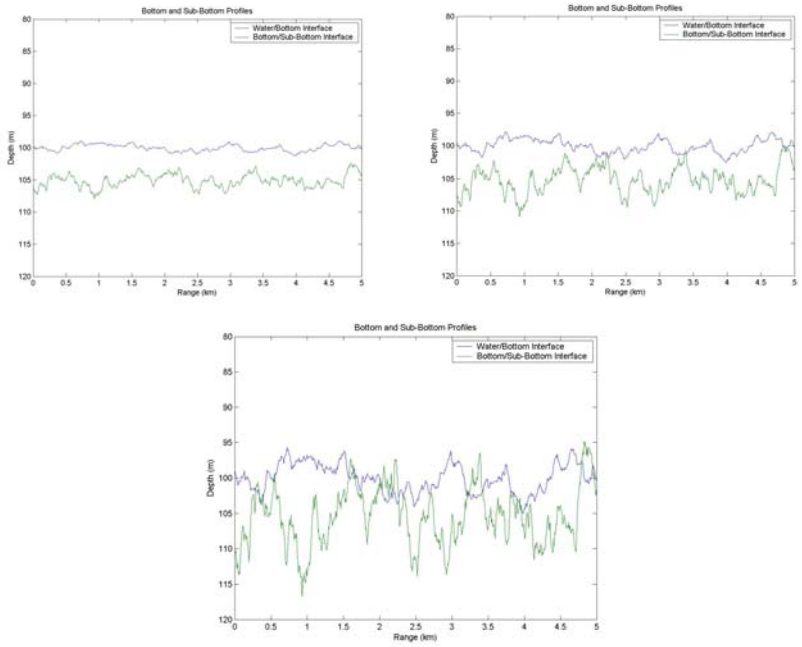

Figure 4. Plots of water/bottom and bottom/sub-bottom interface profiles for increasing rms roughness. (top right) 0.5m & 1m; (top left) 1m & 2m; (bottom) 2m & 4m (water/ bottom and bottom/sub-bottom rms roughness respectively)

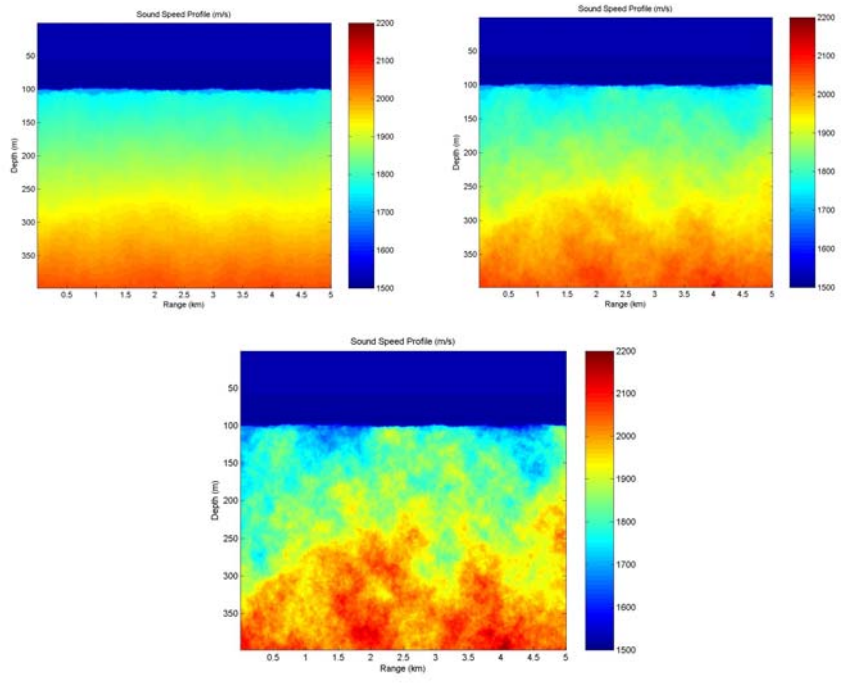

Figure 5. Plots of environmental sound speed for increasing bottom volume sound speed perturbation. (top left) 5 m/s; (top right) 15 m/s; (bottom) 45 m/s rms perturbation

c. Water Volume Turbulence

Five variations in water volume sound speed turbulence were generated as well. In this case, the reference condition is an environment with no water volume sound speed turbulence. The four additional realizations were for increasing degrees of turbulence, specifically 0.5m/s, 1m/s, 2.5m/s, and 5 m/s rms water volume sound speed turbulence. Graphical representations of the four non-reference realizations are depicted in Figure 6.

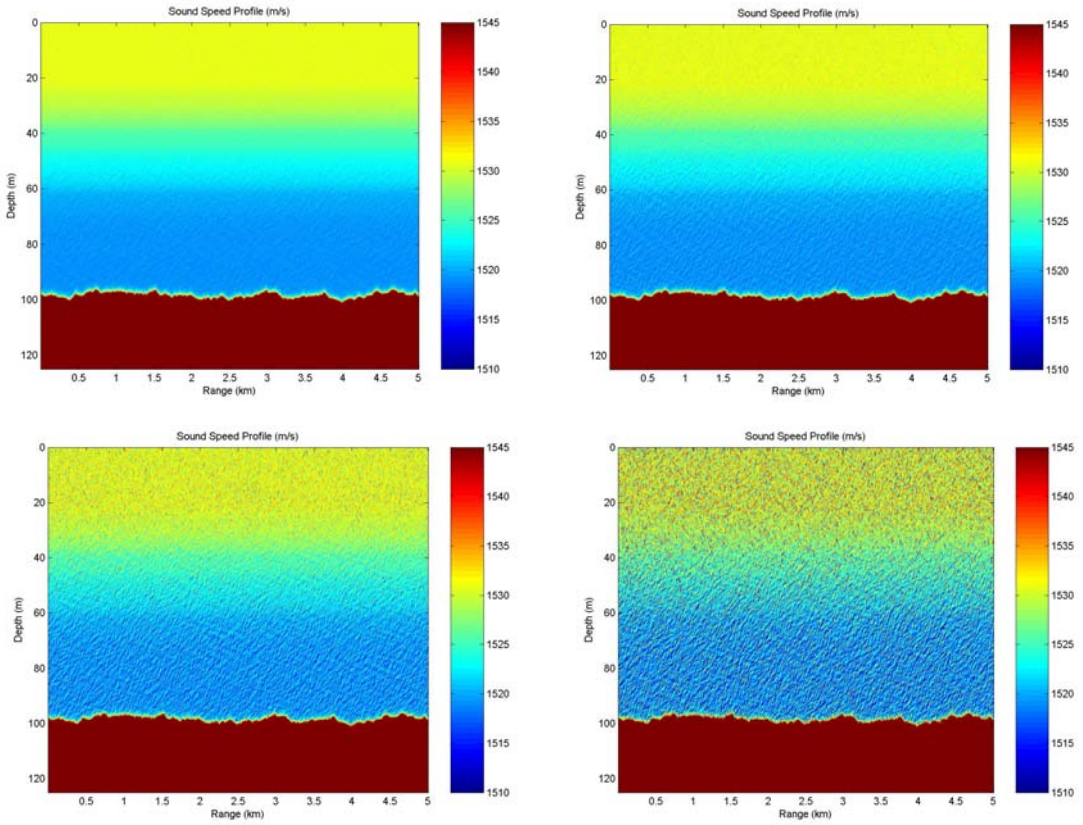

Figure 6. Plots of environmental sound speed for increasing water volume sound speed turbulence. (top left) 0.5 m/s; (top right) 1 m/s; (bottom left) 2.5 m/s; (bottom right) 5 m/s rms turbulence

3. Source Spectra

The output of the MMPE model is the frequency domain response of the field over the specified bandwidth. The source strength for each frequency bin is the same, which may be considered like a square spectrum. Despite the fact that the explosive sources used in ASIAEX are wide band sources, their expected frequency spectrum is not flat. The actual frequency spectra for the explosive charges used in ASIAEX are not

available, but the explosive spectrum for a Standard Underwater Source (SUS) charge for the same size (38g) and detonation depth may be modeled as depicted in Figure 7. The spectrum for a 1kg SUS charge is very similar.

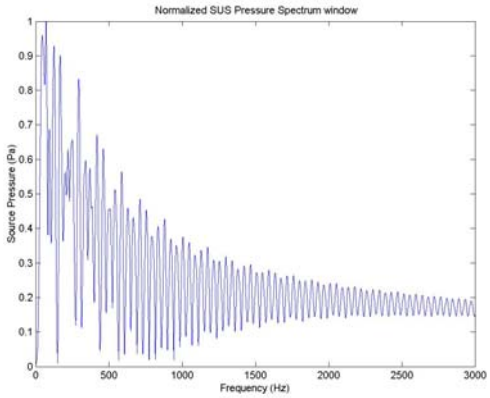

Figure 7. Normalized Expected SUS Pressure Amplitude Spectrum (at 1m from source) for 38g charge exploded at a depth of 48m

In previous theses,[5], [6], [7] a Hanning window spectrum was applied to the output of the MMPE Model. Though this spectrum is advantageous from a signal processing standpoint, it does not approximate the spectrum expected from an explosive charge well. Instead, the SUS spectrum over the calculated bandwidth is applied over the MMPE model output. This is conducted as a multiplication in the frequency domain. However, a direct comparison with previous results is useful, so a separate set of calculations applies a Hanning window to the MMPE Model output as well.

To capture a large portion of the acoustic energy a 500 Hz bandwidth with a 350 Hz center frequency calculated over 1024 frequencies was chosen for the analysis. To approximate an explosive source as used in ASIAEX, the spectrum for a 38g charge exploded at 48m was applied. For comparison with the frequency band used in previous work, a 250 Hz bandwidth with a 250 Hz center frequency calculated over 512 frequencies was also analyzed. To make a closer analysis of the effect of changing the center frequency, a 250 Hz bandwidth with a 350 Hz center frequency also calculated over 512 frequencies was analyzed as well. Both the SUS charge spectrum and a Hanning window were applied to each of these three bands for a total of six variations. These six applied spectra are depicted in Figures 8, 9, and 10. Only the 500 Hz

bandwidth SUS spectrum band was used in calculations for conditions other than the reference.

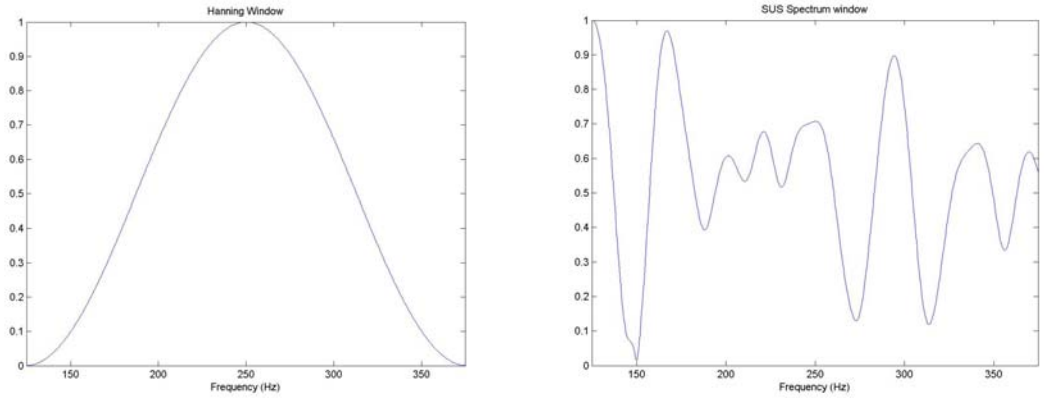

Figure 8. Hanning and Normalized SUS Spectrum Windows for 250 Hz Bandwidth, 250 Hz Center Frequency

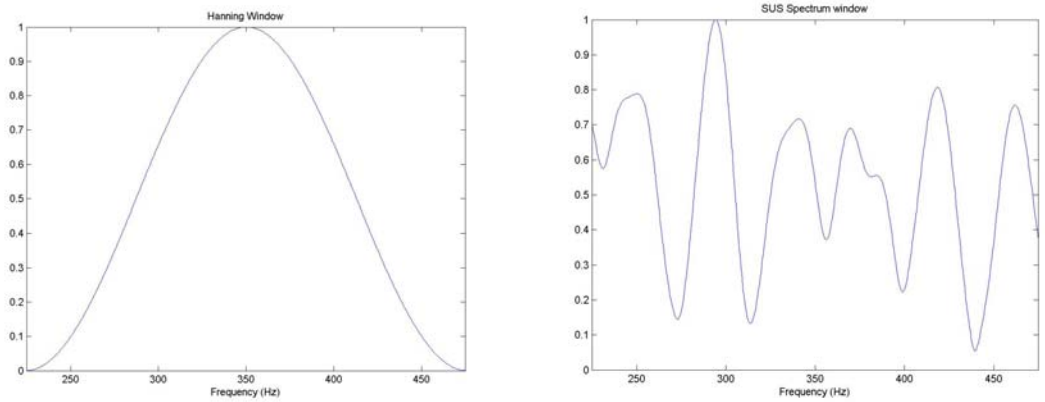

Figure 9. Hanning and Normalized SUS Spectrum Windows for 250 Hz Bandwidth, 350 Hz Center Frequency

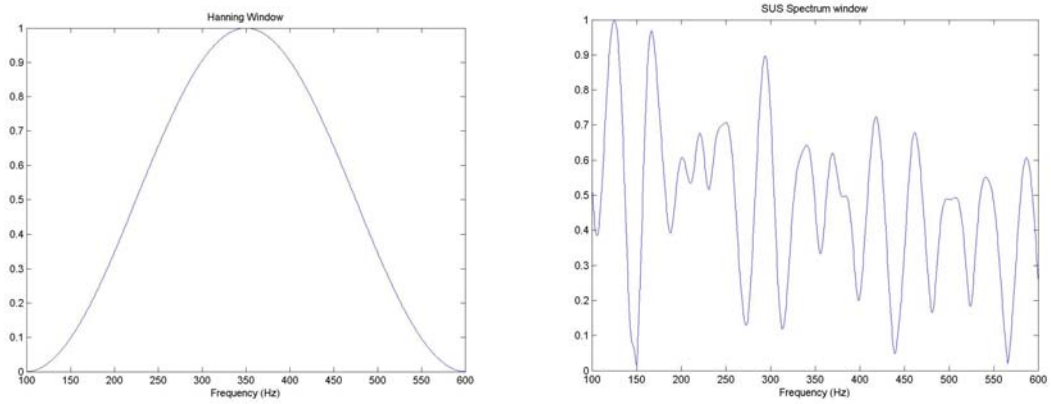

Figure 10. Hanning and Normalized SUS Spectrum Windows for 500 Hz Bandwidth, 350 Hz Center Frequency

4. MMPE Input Parameters

Seven different input files are used to define the desired problem parameters when running the MMPE Model. The information in these input files define the characteristics of the environment, source, receiver, and the resolution of the calculations. The parameters used in these input files for the numerical analysis are provided in Table 1

Filename/Parameter	Value	Remarks
Main Control File: pefiles.inp		
Number of depth points	256	Radix-2 integer required for FFT
Minimum depth	0 m	
Maximum depth	400 m	
Number of range steps	833	
Minimum range	0 m	
Maximum range	5.0 km	
Range step size	6 m	
Maximum computed depth	400 m	
Reference sound speed	1500 m/s	
Source File: pesrc.inp		
Source depths	Varying	Array elements at 20, 24, 28, 32, 36, 40, 44, 48, 52, 56, 60, 64, 68, 72, 76 and 80 m depths.
Center frequency	2 sets	250 Hz and 350 Hz
Frequency bandwidth	2 sets	250 Hz used for both input center frequencies. 500 Hz also used for 350 Hz center frequency in a separate run.
No. of Frequencies	2 sets	1024 for 500 Hz bandwidth, 512 for 250 Hz bandwidth. Radix-2 integer required for FFT
Sound Speed File: pessp.inp		
Water column sound speed	2 sets	SSPAvg & SSPPrevious Range independent
No. of SSPs points	2 sets	84 for SSPAvg & 58 for SSPPrevious
Bathymetry: pebath.inp		
Mean bottom depth	100 m	Range-independent mean
No. of depth points	1	
Bottom properties: pebotprop.inp		
Bottom sound speed	1700 m/s	Mean value
Sound speed gradient	1 /s	Mean value
Relative density	1.6	No density variation
Compressional attenuation	0.15 dB/km/Hz	
Shear speed	0	Negligible
Shear attenuation	0	Negligible

Filename/Parameter	Value	Remarks
Sub-Bottom Bathymetry: pedbath.inp		
Mean Bottom Depth	105 m	Range-independent mean
Sub-Bottom Properties: pedbotprop.inp		
Sub-bottom sound speed	1760 m/s	Mean value
Sound speed gradient	1	Mean value
Relative density	2	Mean value
Compressional attenuation	0.2 dB/km/Hz	
Shear speed	150	Constant
Shear attenuation	0.5	Constant
RMS Perturbations (input during MMPE run)		
Water/bottom interface roughness	3 sets	0.5m, 1m, and 2m
Bottom/sub-bottom interface roughness	3 sets	1m, 2m, and 4m
Bottom Volume sound speed fluctuation	3 sets	5m/s, 15m/s, and 45m/s
Water Volume sound speed fluctuation	4 sets	0.5m/s, 1m/s, 2.5m/s, and 5 m/s

Table 1 MMPE Input Parameters

THIS PAGE INTENTIONALLY LEFT BLANK

IV. DATA ANALYSIS AND RESULTS

A. MMPE MODEL RESULTS

1. Time Domain Reverberation Analysis

In the previous chapter, the method of time domain analysis of the reverberation loss for the interfaces and the bottom volume was described. To calculate the structure of the reverberation loss, *RL',* from the interfaces in a more standard dB scale, the output from the MMPE Model and post-processing is adjusted by

$$RL'_b(t_n) = -20\log\left[\left|p_{-b}(t_n)\right|\right], \tag{99}$$

where $p_{-b}(t_n)$ is the interface (either one) reverberation pressure at the receiver calculated in Eq. (94). Similarly, reverberation loss structure from the bottom volume is determined by

$$RL'_v(t_n) = -20\log\left[\left|p_{-v}(t_n)\right|\right], \tag{100}$$

where $p_{-v}(t_n)$ is the bottom volume reverberation pressure at the receiver calculated in Eq. (98). In either case, the result is the predicted reverberation loss structure from either of the interfaces or the bottom volume. It should be noted that this method predicts reverberation loss structure and not actual levels since we are neglecting the actual scattering strengths.

Typical predicted reverberation loss structures for both interfaces and the bottom volume are depicted in Figure 11. The source depth used for all of the numerical analysis is 48m. A receiver depth of 40m is chosen to display typical predicted reverberation loss structures in this figure and all of the reverberation loss structure plots that follow. Unless otherwise stated, the applied source spectrum is the broadband, SUS spectrum source with a center frequency of 350 Hz and a bandwidth of 500 Hz calculated over 1024 frequency bins.

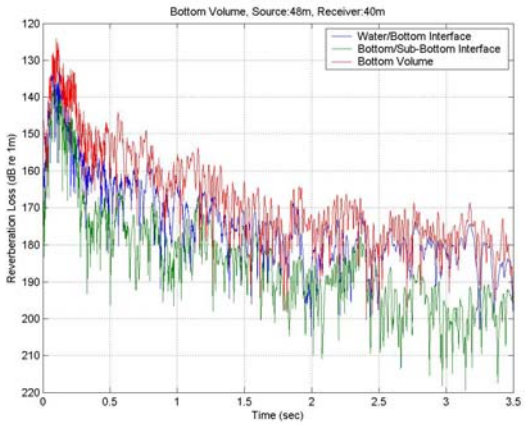

Figure 11. 500 Hz bandwidth, 350 Hz center frequency, SUS spectrum reverberation loss curves for "reference" environment for source at 48 m and receiver at 40 m

The purpose of performing this numerical analysis is to generate a prediction of the expected spatial coherence in the vertical direction for an environment and problem geometry similar to that observed in ASIAEX. To determine the spatial coherence from the MMPE Model outputs, a cross correlation method is used. In this method, the normalized cross correlation of the interface reverberation pressures, $p_{-b}(t_n)$, for the source and each receiver is performed. To generate a peak value in dB, the maximum of $20\log\left(\left|xcorr\right|\right)$, where *xcorr* is the output of the normalized cross correlation, is determined. This is repeated for all 16 elements and plotted for both interfaces and the volume to generate an expected spatial coherence.

It should be noted that all correlation curves, unless otherwise stated, are based on a single environmental realization. Ideally, multiple random realizations should be computed to create average correlation curves. However, due to the calculation times of the model, such an approach is prohibitive.

2. Influence of Interface Roughness Variation

Plots of the predicted reverberation loss structures for all 3 variations in interface roughness are plotted in Figure 12. Variation in interface roughness appears to have no strong effect on the reverberation loss structure for either of the interfaces or the bottom volume. This conclusion is consistent with the results of previous thesis work[7] for the water/bottom interface and the bottom volume. A slight increase in reverberation

pressure level with an increase in the rms roughness value, which is particularly apparent for the bottom/sub-bottom interface in the previous work, is not evident here.

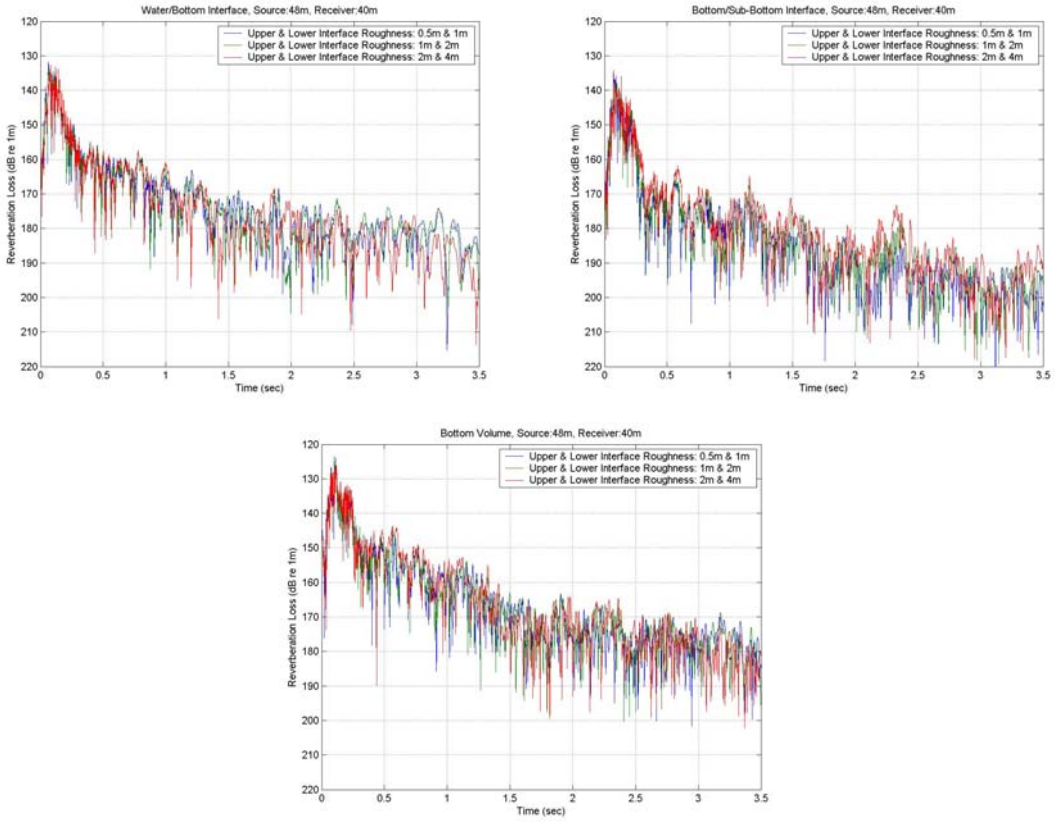

Figure 12. Reverberation loss curves for three variations in interface roughness. (top left) water/bottom interface; (top right) bottom/sub-bottom interface; (bottom) volume

The corresponding peak vertical correlation plots are depicted in Figure 13. For both the water/bottom interface and the bottom volume, variations in interface roughness have very little effect. The bottom/sub-bottom interface displays some difference in peak vertical correlation at the upper and lower edges of the array. A clear overall trend with variations in bottom roughness is not apparent for either of the interfaces or the bottom volume. As with the reverberation loss structure, the results for the water/bottom interface and the bottom volume are similar to those of the previous thesis. However, a clear decrease in vertical correlation with increasing roughness was previously seen[7] for the bottom/sub-bottom interface, and that trend is not seen here.

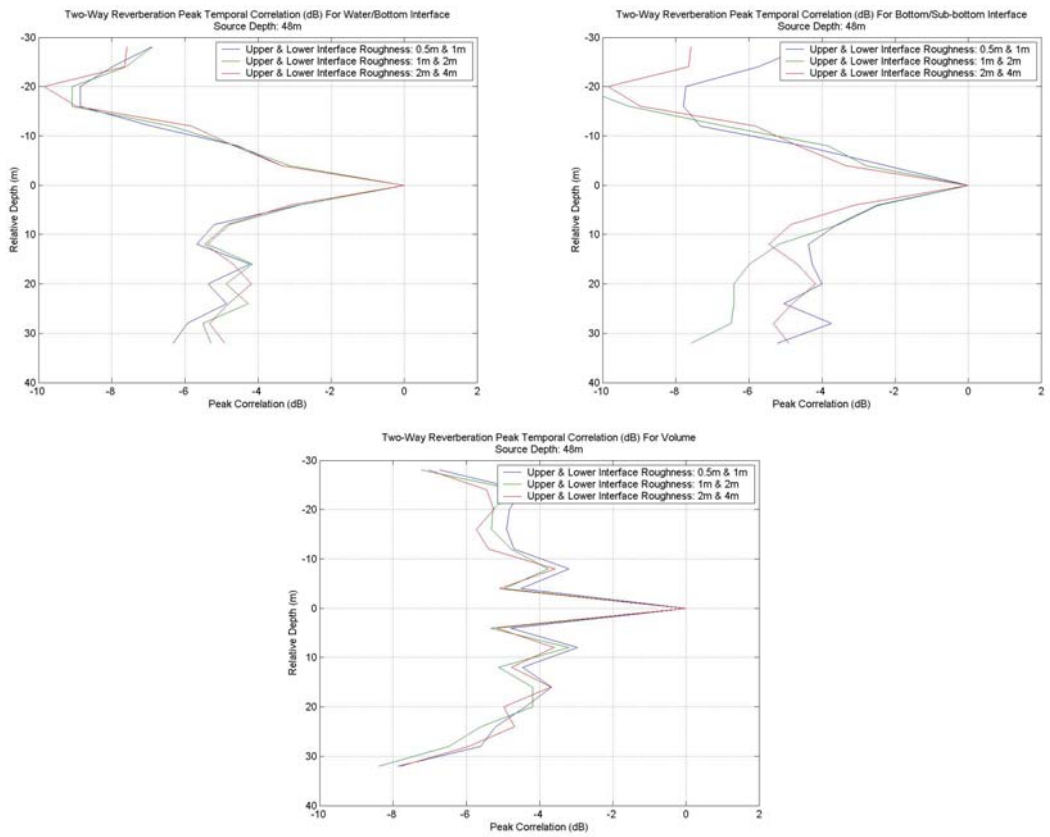

Figure 13. Peak vertical correlation curves of reverberation loss for three variations in interface roughness. (top left) water/bottom interface; (top right) bottom/sub-bottom interface; (bottom) volume

3. Influence of Bottom Sound Speed Perturbations

Plots of the predicted reverberation loss structures for all 3 variations in bottom sound speed perturbations are plotted in Figure 14. For both interfaces and the bottom volume, a clear increase in reverberation loss with an increase in bottom sound speed rms perturbation value is shown. The previous thesis[7] displayed the same trend in all three cases, though to a larger degree. This trend is probably caused by an increase in the scatter of acoustic energy to deeper depths at shorter ranges caused by the larger bottom volume perturbations.

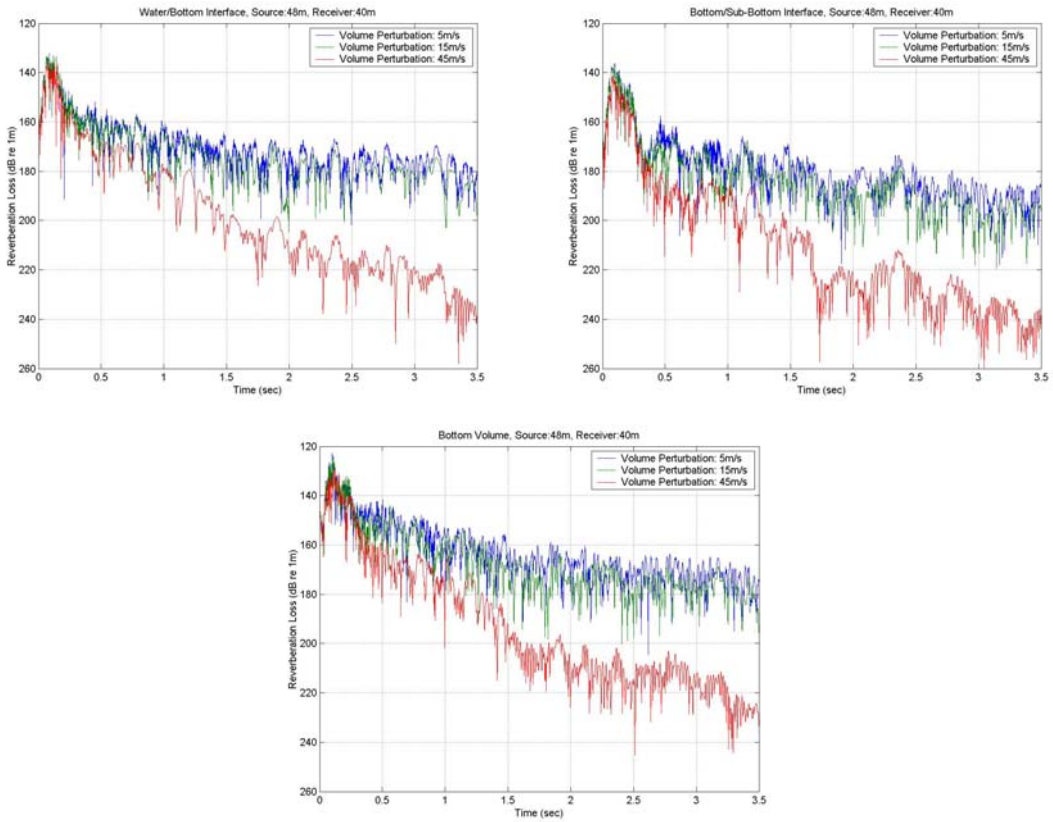

Figure 14. Reverberation loss curves for three variations in bottom volume sound speed perturbation. (top left) water/bottom interface; (top right) bottom/sub-bottom interface; (bottom) volume

The corresponding peak vertical correlation plots are depicted in Figure 15. Except for the largest bottom sound speed rms perturbation value, there is little change in the peak vertical correlation. For the bottom volume, even the largest rms perturbation value does not have a significant effect. Once again, these results are similar to those of the previous thesis. The effect of the highest perturbation can be considered an anomaly since it produces unrealistic regions where bottom volume sound speed drops below that of the water volume, allowing a large amount of acoustic energy to transmit directly across the interface into the bottom, where it is mostly lost. Except for this unrealistic case, it appears that variations in bottom sound speed perturbations have little influence on peak vertical correlation.

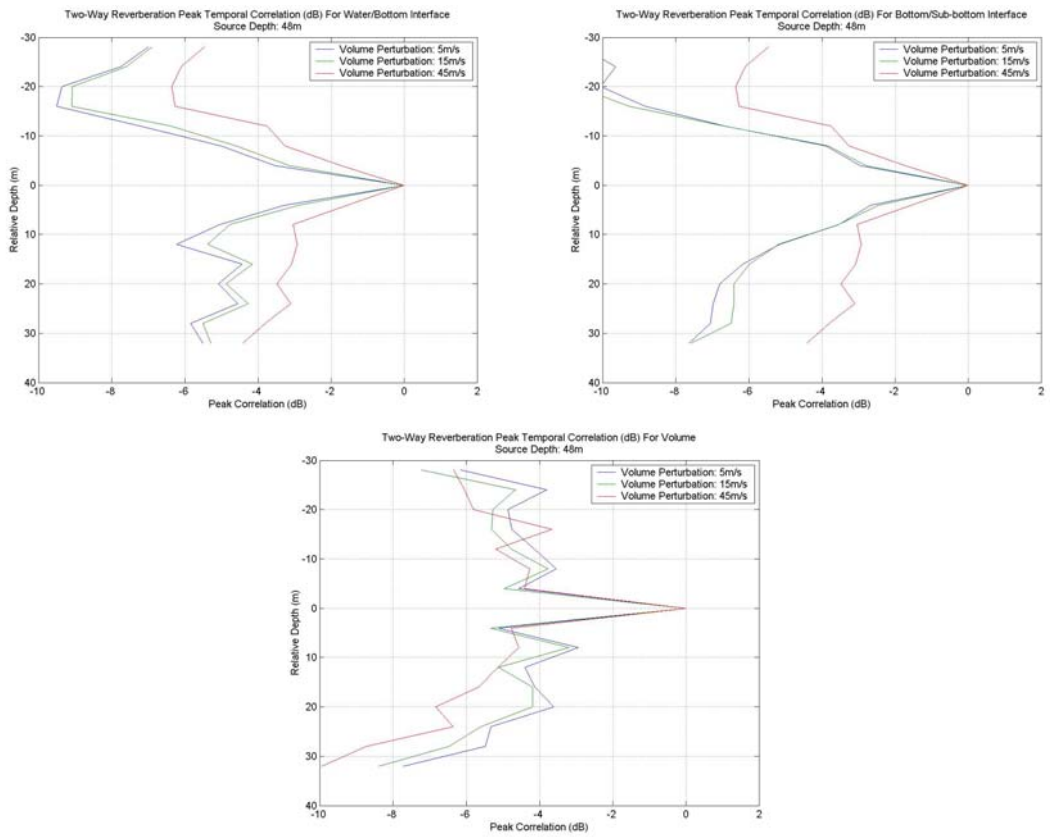

Figure 15. Peak vertical correlation curves of reverberation loss for three variations in bottom volume sound speed perturbation. (top left) water/bottom interface; (top right) bottom/sub-bottom interface; (bottom) volume

4. Influence of Water Volume Sound Speed Turbulence

Plots of the predicted reverberation loss structures for all 5 variations in water sound speed turbulence are plotted in Figure 16. In this case, only the reverberation loss for the two interfaces was processed. Plots of the difference between the reverberation loss structure for the reference environment, which contained no water volume sound speed turbulence, and the 4 increased rms turbulence values are included in this figure to better represent the small influence of increased sound speed turbulence. A close look at these difference plots shows that the generally small difference between the reference and more turbulent environments also maintains its own structure over different turbulence values. This is probably an artifact caused by the use of the same water volume sound speed realization modified by a scaling parameter to generate the different turbulent fields.

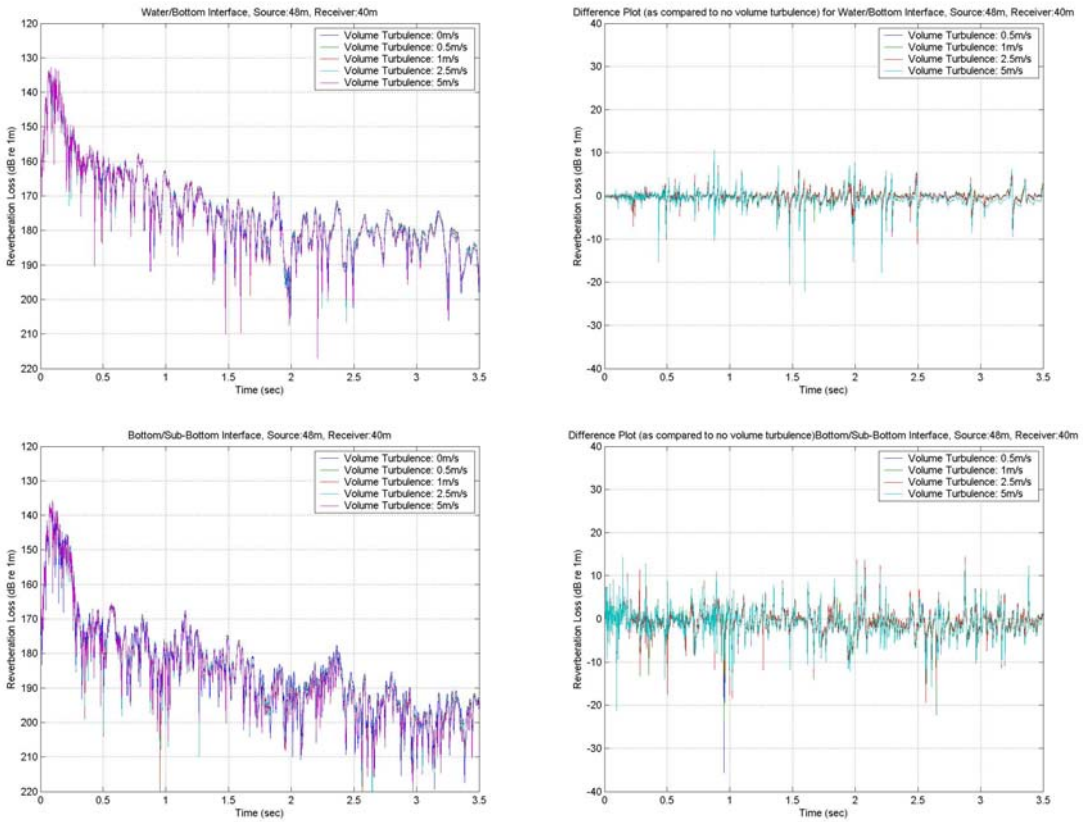

Figure 16. Reverberation loss curves and difference plots for five variations in water volume sound speed turbulence. (top) water/bottom interface RL plot and difference plot; (bottom) bottom/sub-bottom interface RL plot and difference plot

The corresponding peak vertical correlation plots are depicted in Figure 17. As with the reverberation loss curves, there is very little difference in peak vertical correlation induced by variations in water volume turbulence for either interface. In fact, the difference between variations in the water/bottom interface is only a small fraction of a dB. Though the influence of turbulence was not accounted for in the previous thesis,[7] these results are very similar to those for moderately small variations in the SVP. With this result in mind, it is apparent that changes in the water volume sound speed of this scale have little influence on either the reverberation loss structure or the peak vertical correlation.

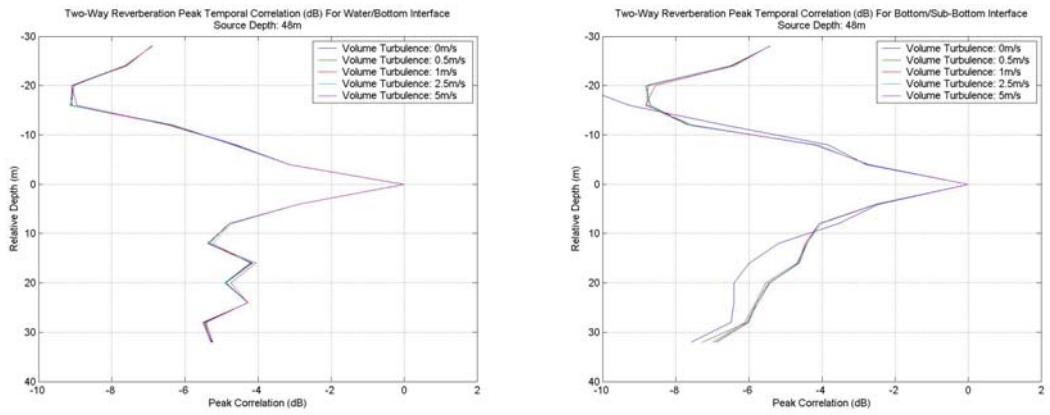

Figure 17. Peak vertical correlation curves and difference plots for five variations in water volume sound speed turbulence. (top) water/bottom interface RL plot and difference plot; (bottom) bottom/sub-bottom interface RL plot and difference plot

5. Influence of Bandwidth

Our goal is to generate a useful model for use as a basis for comparison for spatial coherence analysis of broadband data. To accomplish this, the numerical analysis must include the peak vertical correlation structure for both interfaces and the bottom volume over several different bandwidths. In this case, a bandwidth reduction to 250 Hz over 512 frequency bins is generated directly by running the MMPE Model for the new spectrum. However, results for even smaller bandwidths are generated by removing the unwanted components from the original interface and bottom volume reverberation pressures, $p_{-b,v}(t_n)$, which generates the reverberation pressures for these new, smaller bandwidths. Reverberation loss and peak vertical correlation are then calculated from these reverberation pressures in the same manner as before.

Reducing the bandwidth from the 500 Hz bandwidth, 350 Hz center frequency SUS spectrum in the reference environment results in the peak vertical correlations depicted in Figure 18. For these new frequency bands, the center frequency remained fixed at 350 Hz, but the bandwidth was reduced to 250 Hz, 125 Hz, and 62.5 Hz. These combinations of bandwidth and center frequency result in increasing fc/BW ratios of 0.7, 1.4, 2.8, and 5.6, respectively. As opposed to the example given in the correlation method theory, no exploitable trend in bottom or interface vertical peak correlation

presents itself. In fact, the only apparent trend is that both interfaces and the volume display somewhat higher levels of peak vertical correlation with decreasing bandwidth.

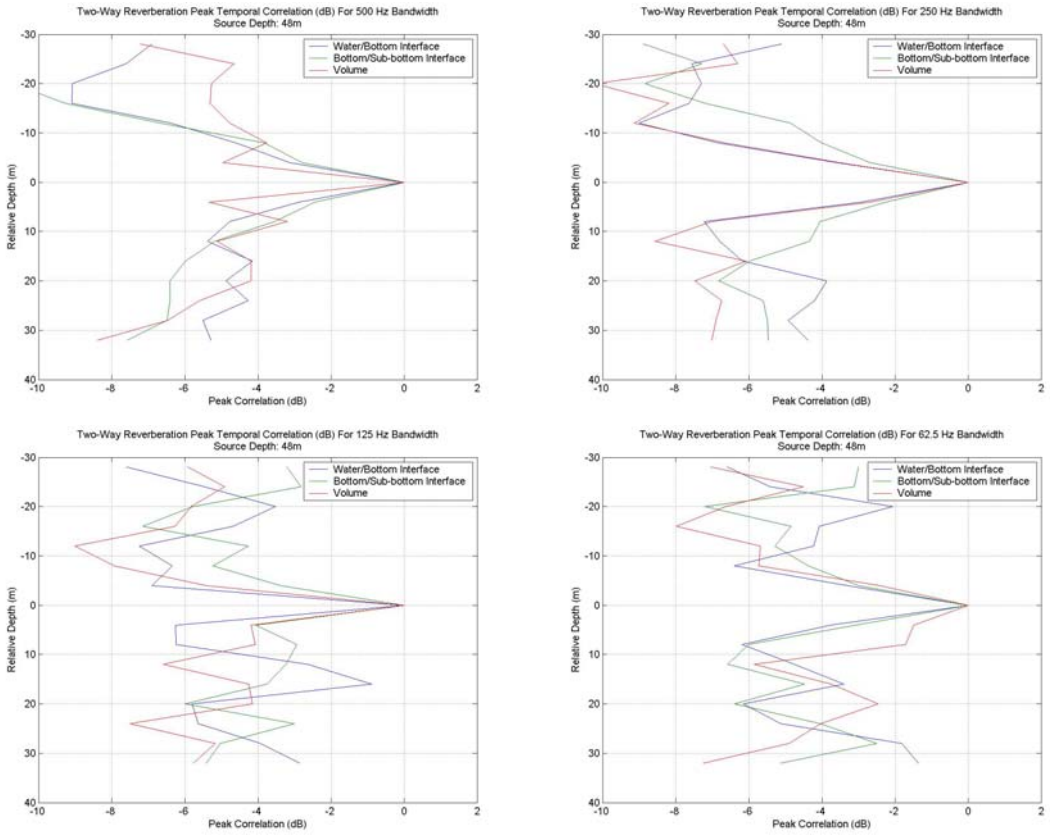

Figure 18. 350 Hz center frequency, SUS spectrum peak vertical correlation curves for four bandwidths. (top left) 500 Hz bw; (top right) 250 Hz bw; (bottom left) 125 Hz bw; (bottom right) 62.5 Hz bw

6. Influence of Source Spectrum

In the previous thesis,[7] similar numerical analysis was conducted using a different source spectrum. In particular, a 250 Hz bandwidth, 250 Hz center frequency Hanning source spectrum was used. For this source spectrum, the peak vertical correlation decreased much more rapidly for the volume than either interface. This suggests that an exploitable difference in the trend in bottom or interface vertical peak correlation with decreasing bandwidth may be found in the numerical analysis if a different source spectrum is used.

The first component of the source spectrum that is changed to test this notion is the applied amplitude spectrum. A Hanning window replaces the SUS spectrum and the

MMPE model is run for the 500 Hz bandwidth, 350 Hz center frequency band in the reference environment. All smaller bandwidth calculations are made in a similar fashion as before. The results of this change in the source are shown in Figure 19. For this case, a trend with decreasing bandwidth can be seen. Despite the fact that peak vertical correlation doesn't appear to change significantly for either interface, peak vertical correlation for the bottom volume is clearly less than that of the interfaces for the 500 Hz bandwidth. As the bandwidth is reduced, peak vertical correlation for the bottom volume increases to the point where it appears similar to the interfaces. This is an exploitable trend.

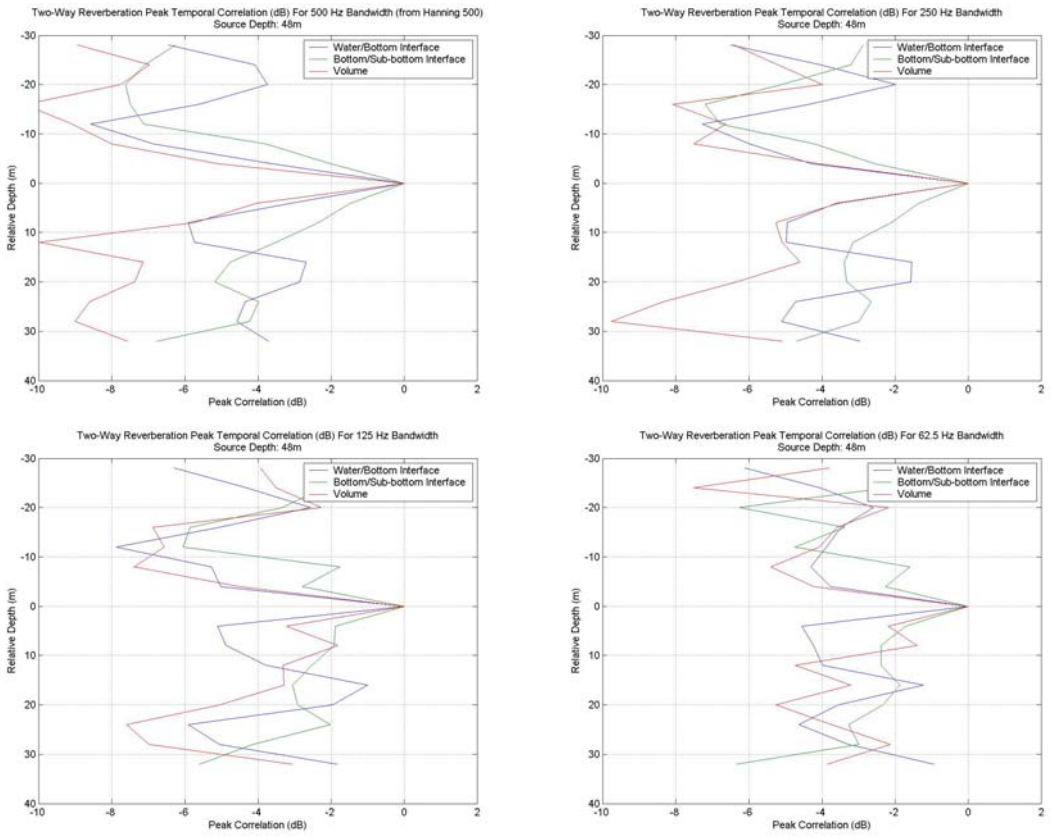

Figure 19. 350 Hz center frequency, Hanning spectrum peak vertical correlation curves for four bandwidths. (top left) 500 Hz bw; (top right) 250 Hz bw; (bottom left) 125 Hz bw; (bottom right) 62.5 Hz bw

The most likely explanation for this change in peak vertical correlation with the source spectrum lies in the structure of the SUS spectrum itself. The SUS spectrum applied to the 500 Hz bandwidth, 350 Hz center frequency case is shown in Figure 20.

Note that several narrow peaks rise above the rest of the frequency weighting values. These peaks are effectively small bandpass filters. In light of this, the mild effect on peak correlation observed for reduced bandwidth when the explosive SUS spectrum is applied is understandable. The output for the larger bandwidths is essentially passed through small bandpass filters already, and further reduction in bandwidth should yield little change.

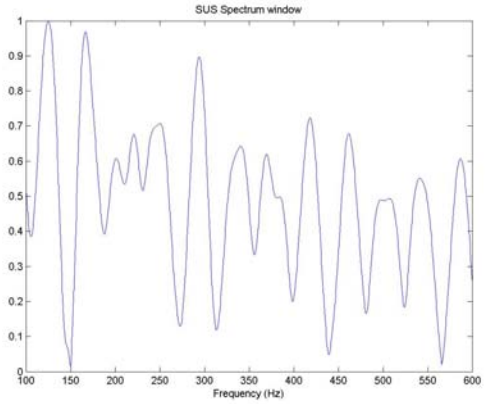

Figure 20. SUS Spectrum for 500 Hz Bandwidth, 350 Hz Center Frequency

7. Influence of Center Frequency

Another difference between the source used in this thesis and the previous thesis is the center frequency. To test the influence of this difference as well, the MMPE model is run for a 250 Hz bandwidth, 250 Hz center frequency SUS spectrum band in the reference environment. The 125 and 62.5 Hz bandwidth calculations are then performed in the same manner as before. A 500 Hz bandwidth is not calculated in this case since it includes the DC (i.e., 0 Hz) and very low frequency (VLF) components that are problematic for the MMPE Model. Note that this change in center frequency results in new fc/BW ratios of 1, 2, and 4, respectively. The results for these bands are shown in Figure 21. As with the 350 Hz centered SUS spectrum, no discernable trends in peak vertical correlation is noted.

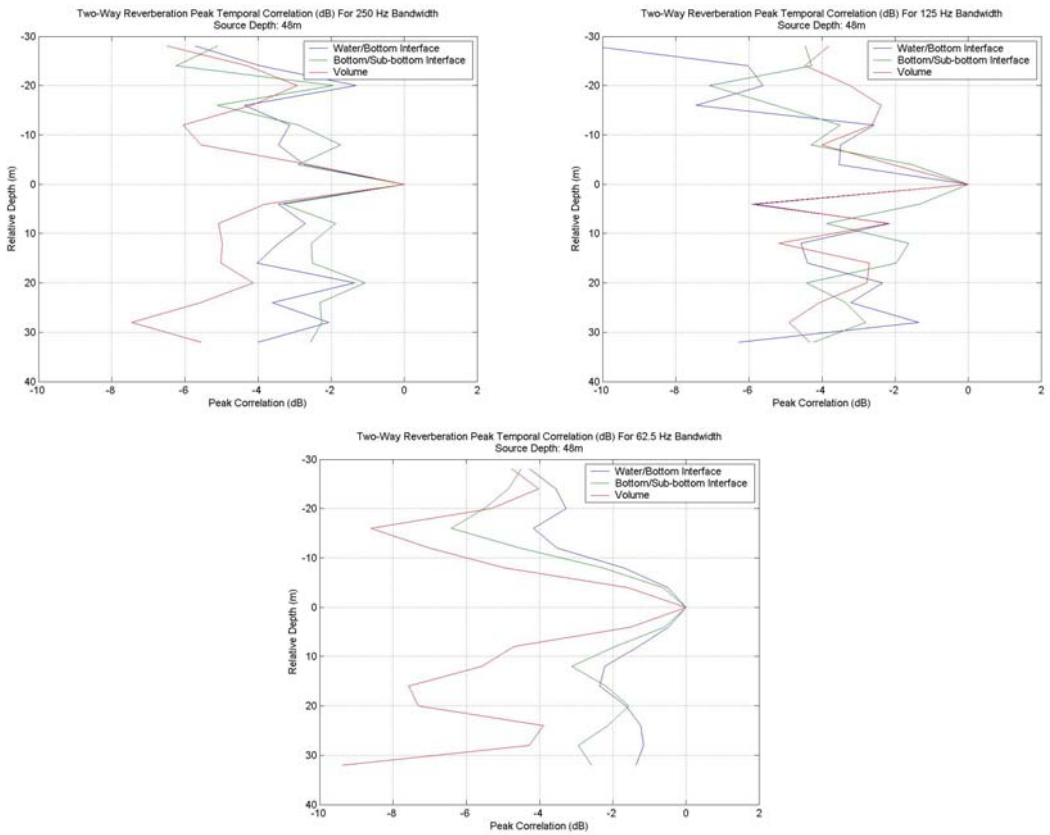

Figure 21. 250 Hz center frequency, SUS spectrum peak vertical correlation curves for four bandwidths. (top left) 250 Hz bw; (top right) 125 Hz bw; (bottom) 62.5 Hz bw

The final source spectrum to be considered is the exact spectrum used in the previous thesis, a 250 Hz bandwidth, 250 Hz center frequency Hanning window spectrum frequency band in the reference environment. The results for this band are shown in Figure 22. As with the 350 Hz centered Hanning window spectrum results, the same clear and exploitable trend is shown. Peak vertical correlation values for both interfaces again remain essentially unchanged, while the peak vertical correlation for the bottom volume is much lower at larger bandwidths and increases to levels close to that of the interfaces with decreasing bandwidth.

It is important to note that, given the right source spectrum, there does appear to be a trend in the vertical coherence results which distinguishes interface and volume reverberation contributions at large bandwidth. This is consistent with the theoretical results of Ivakin.[13] However, in contrast to the theory, the numerical analysis suggests

that a decrease bandwidth tends to increase the coherence of the volume reverberation. The cause of this discrepancy is unknown, but possible influences from the propagation could be the multipath structure and/or the background sound speed gradient in the bottom volume. Analysis of the impact of these phenomena remains for future work.

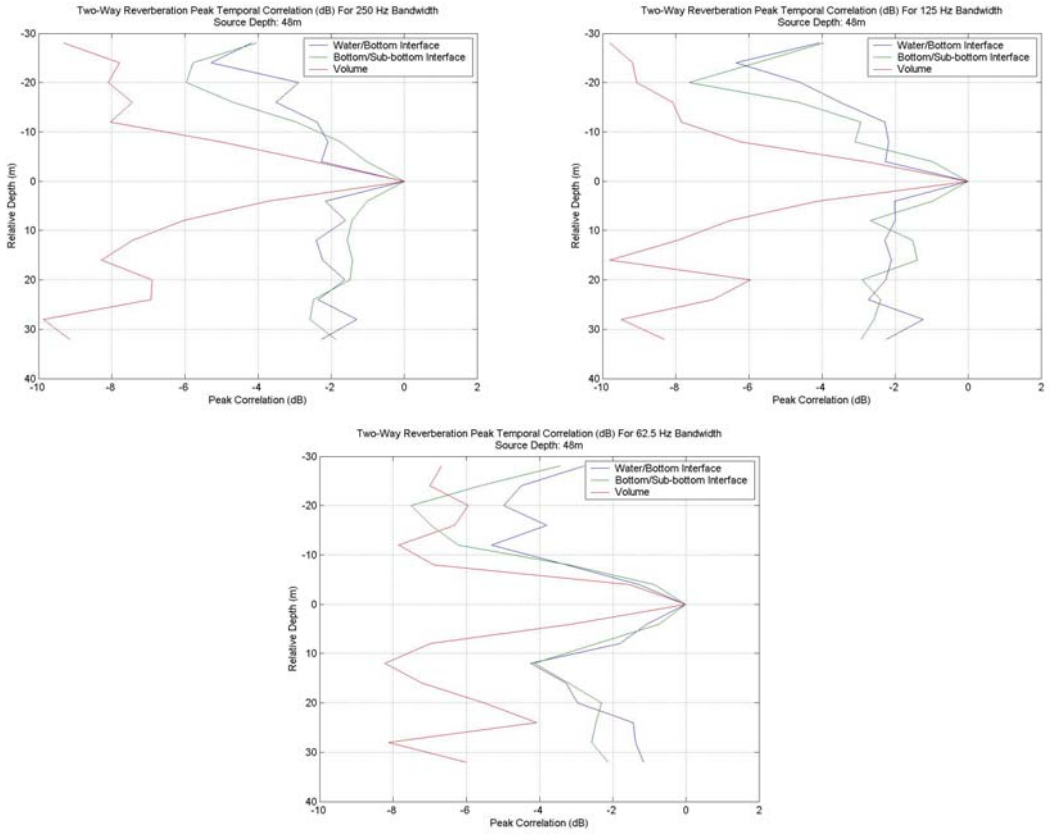

Figure 22. 250 Hz center frequency, Hanning spectrum peak vertical correlation curves for four bandwidths. (top left) 250 Hz bw; (top right) 125 Hz bw; (bottom) 62.5 Hz bw

B. ASIAEX DATA RESULTS

1. General Results

Among the experiments that were conducted during the ASIAEX, one set of experiments involved deploying explosive charges from the research vessel *Shiyan-3*. The reverberation from the shallow water environment was then recorded by a vertical array that was suspended from the ship. The recorded signals form a data set from nine 38g charges and four 1kg charges. Received signals were digitally recorded at a sampling frequency of 6000Hz.

To record the reverberant signals, a 32 element vertical array, designated VLA1, was employed. This array spanned the majority of the water column, covering about 86m of its 100m depth. The spacing of the elements of this array was semi-irregular as shown in Table 2. Two of these elements malfunctioned during the experiment, I-11 and I-15, and the recordings from these elements were not used in the data analysis. An index number was assigned to the remaining 30 working elements, which is used in some of the figures that follow.

Hydrophone	Depth	Spacing	Remarks	Hydrophone	Depth	Spacing	Remarks
I-32	4.60m	-	Index 30	I-16	32.50m	2.00m	Index 14
I-31	6.33m	1.73m	Index 29	I-15	36.50m	4.00m	Bad element
I-30	8.13m	1.80m	Index 28	I-14	40.50m	4.00m	Index 13
I-29	10.21m	2.08m	Index 27	I-13	44.50m	4.00m	Index 12
I-28	11.69m	1.46m	Index 26	I-12	48.50m	4.00m	Index 11
I-27	13.35m	1.66m	Index 25	I-11	52.50m	4.00m	Bad element
I-26	15.02m	1.67m	Index 24	I-10	56.50m	4.00m	Index 10
I-25	16.81m	1.79m	Index 23	I-9	60.50m	4.00m	Index 9
I-24	18.61m	1.80m	Index 22	I-8	64.50m	4.00m	Index 8
I-23	20.38m	1.77m	Index 21	I-7	68.50m	4.00m	Index 7
I-22	21.96m	1.58m	Index 20	I-6	72.50m	4.00m	Index 6
I-21	23.68m	1.72m	Index 19	I-5	76.50m	4.00m	Index 5
I-20	25.36m	1.68m	Index 18	I-4	80.50m	4.00m	Index 4
I-19	27.06m	1.70m	Index 17	I-3	82.50m	2.00m	Index 3
I-18	28.75m	1.69m	Index 16	I-2	86.50m	4.00m	Index 2
I-17	30.50m	1.75m	Index 15	I-1	90.50m	4.00m	Index 1

Table 2 Element Spacing and Depth for Vertical Array VLA1 Used in ASIAEX

An unexpected difference in the recorded signals between different elements was discovered early in the analysis. The recorded signals from the lower 16 elements of VLA1, I-1 through I-16, displayed a different received signal shape than signals from the upper 16 elements, I-17 through I-32. An example of this difference from the first 38g charge for the two adjacent elements of these two 16 element sets is shown in Figure 23. Further analysis shows that the signals from the upper elements contain stronger low frequency components than the signals recorded by the lower elements. Element placement within the water column should not account for this difference, as I-16 and I-17 are only 2m apart. Instead, it has been confirmed that the settings for these two 16

element sets were indeed different, though the exact nature of this difference remains unknown.

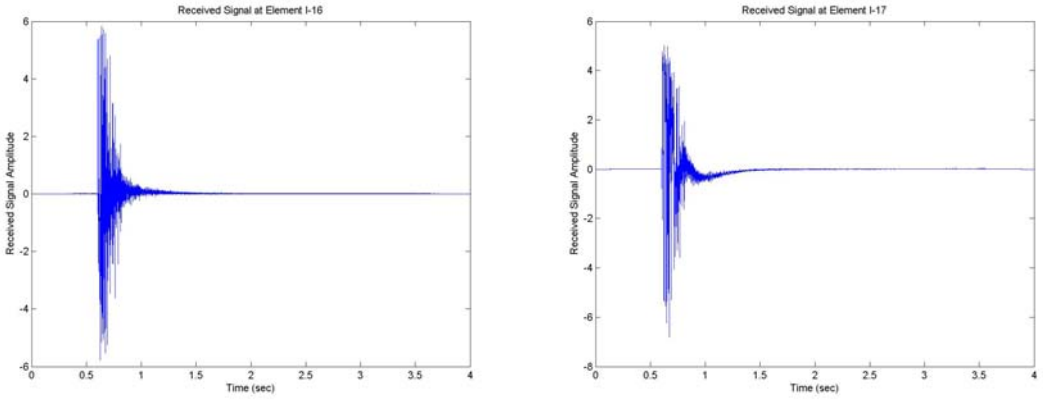

Figure 23. Two Received Signals From the First 38g Charge.

Plots for the received signals recorded by the same two elements, I-16 and I-17, for the first 1kg charge are shown in Figure 24. The difference in the shape of the received signals from the two halves of the array is still quite evident. These plots also reveal that the signals recorded from this charge display a large amount of clipping. This was present in all four of the 1kg charge recordings. Some signal clipping was also evident in the recorded signals for the final three 38g charges.

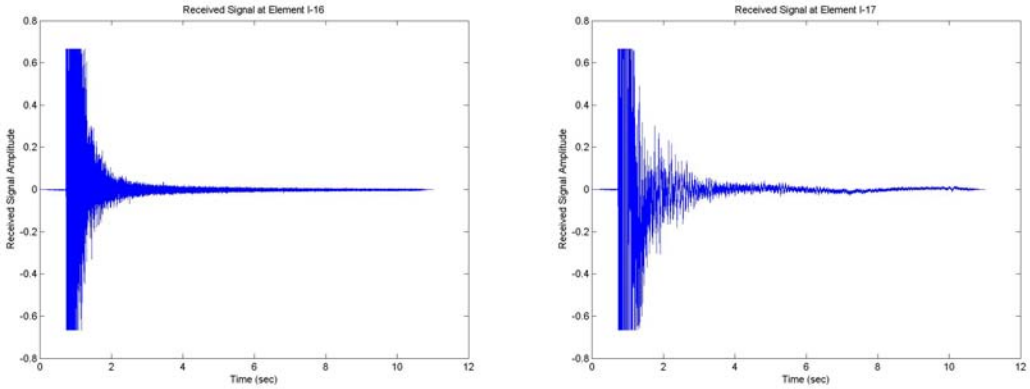

Figure 24. Two Received Signals From the First 1kg Charge.

Vertical peak correlation for the recorded data is determined in a manner similar to that used for the numerical analysis results. In this case there is no clear reference element since none of the elements corresponds directly to the source. Instead, the normalized cross correlation of all 30 working elements is performed with respect to each

of the others. The maximum value of each of these cross correlations is determined to form a 30x30 matrix of peak correlation values. These peak normalized cross correlation values are then converted to a dB scale in the same manner as before, $20\log\left(\left|xcorr\right|\right)$.

Two methods are used to display the peak vertical correlation results for the ASIAEX data. Due to the semi-irregular spacing of VLA1, the relative spacing between elements rarely aligned, making a spatial average impossible to determine. Instead, the plots of peak vertical correlation with respect to all 30 working elements are superimposed on the same plot against an axis of the relative depth difference between elements for each correlation calculation. To visually sort this wealth of information, an image plot is also generated where the peak correlation matrix is displayed as an image with color-coding representing the numerical correlation value in dB. Note that the autocorrelation values run diagonally through the image. The axes of this plot use the previously defined element index number from Table 2. An example of both plot types for the first 38g charge is shown in Figure 25.

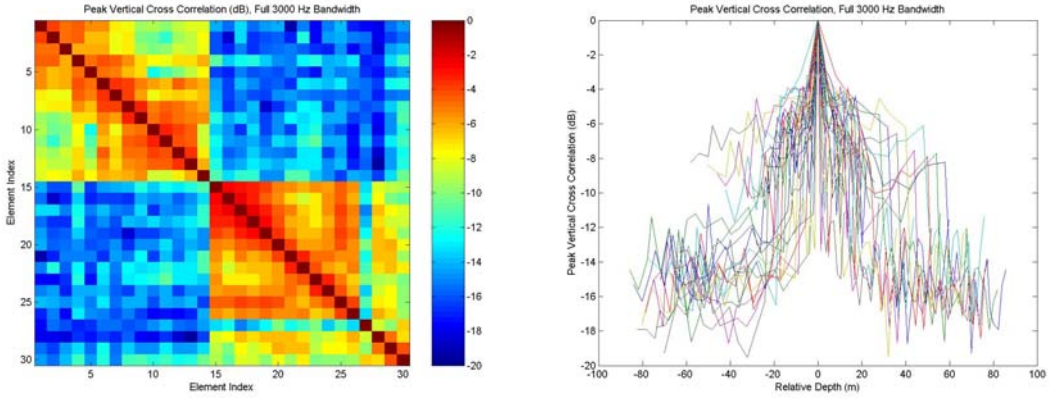

Figure 25. Peak Vertical Correlation Between Elements For 38g Charge

The effect of the difference in the recorded signals between the upper and lower portions of the array can be clearly seen in the image plot in Figure 25. Peak vertical correlation values are much higher between elements of the same half of the array than they are between elements in different halves of the array. In further analysis, the received signals are filtered using a bandpass filter prior to conducting the cross correlations. For bands that contain DC and the low frequency components, the bi-polar structure seen in the full spectrum analysis is still present. For bands that remove these

low frequency components, the bi-polar structure is absent and peak vertical correlation values are generally lower overall (though significantly higher between elements located in different halves of the array). Examples of this trend are evident when Figure 25 and 26 are compared.

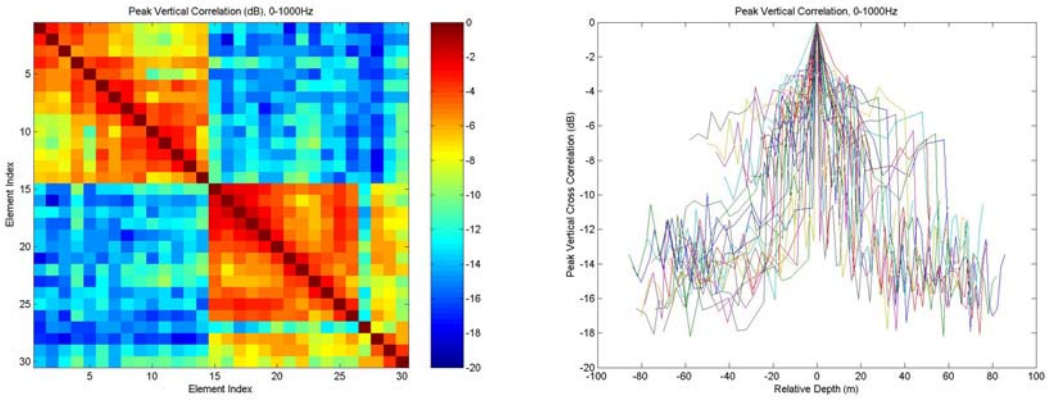

Figure 26. Peak Vertical Correlation Between Elements For 38g Charge, 0-1000 Hz Band

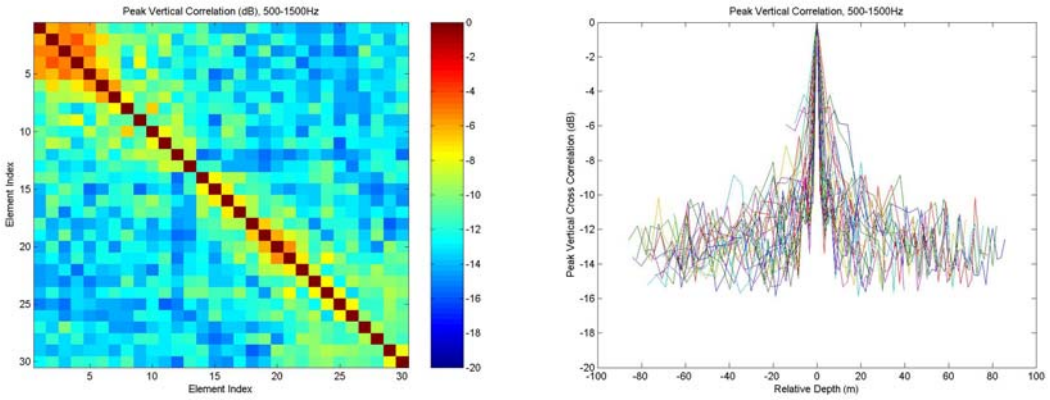

Figure 27. Peak Vertical Correlation Between Elements For 38g Charge, 500-1500 Hz Band

To this point, only examples for the 38g charges have been displayed. The same plot types as shown above are displayed for the first 1kg charge in Figures 28, 29, and 30. In general, the same trends are apparent for the larger explosive charges as were seen for the 38g charges. Overall peak vertical correlation values are much lower for these 1kg charges than for their 38g counterparts. This is probably a result, at least in part, of the large amount of signal clipping observed. The high correlation between elements in the upper portion of the array relative to the elements of the lower portion of the array for bands that contain DC and low frequencies is generated by the differences in the recorded

signals in these two halves of VLA1. Due to this low correlation, the remaining analysis will focus on the 38g charges.

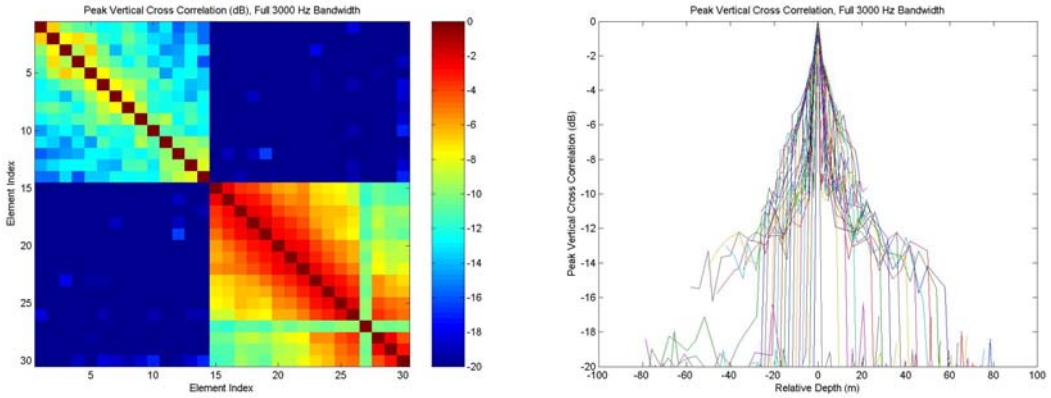

Figure 28. Peak Vertical Correlation Between Elements For 1kg Charge

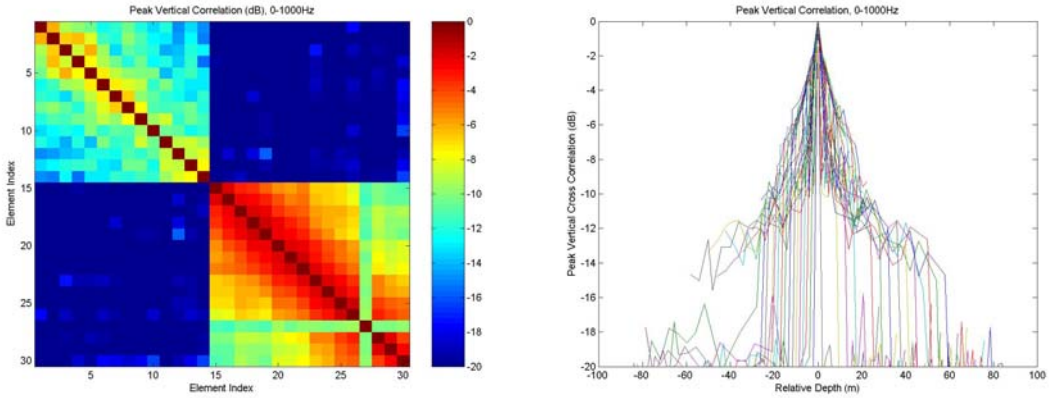

Figure 29. Peak Vertical Correlation Between Elements For 1kg Charge, 0-1000 Hz Band

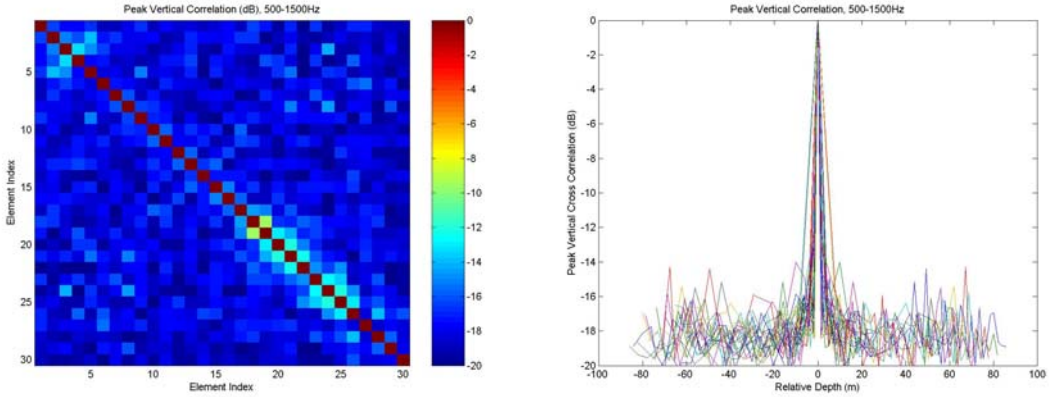

Figure 30. Peak Vertical Correlation Between Elements For 1kg Charge, 500-1500 Hz Band

A closer analysis of the 38g charges reveals that each charge displays particularly high peak vertical correlation values in the vicinity of 100 Hz. For each charge, the specific center frequency for which a band displays the highest peak vertical correlation is given in Table 3. No strong environmental source is observed at or near these frequencies prior to the recorded explosion. The cause of this region of high vertical correlation could be an artifact of the array, the recording equipment, or an oddity in the environment. An attempt to remove the explosive source spectrum from the recorded signal using a similar SUS spectrum generated in the same manner as in the numerical analysis failed to remove this region of high vertical correlation, but this result is far from conclusive. It should be noted that the numerical analysis does not include frequencies of 100 Hz or below, so the effect of this high correlation region on comparison between data and numerical analyses is minimal.

Charge Number	High Correlation Center Frequency	Charge Number	High Correlation Center Frequency
1	80 Hz	6	90 Hz
2	105 Hz	7	85 Hz
3	105 Hz	8	90 Hz
4	80 Hz	9	95 Hz
5	80 Hz		

Table 3 High Peak Vertical Correlation Center Frequencies for 38g Charges

2. Influence of Bandwidth on Peak Vertical Correlation

The results of the numerical analysis showed that, for a broadband explosive (SUS) source, there was no exploitable trend with decreasing bandwidth observed between the peak vertical correlation values from reverberation caused by the interfaces and that caused by the bottom volume. In fact, the only trend in peak vertical correlation with decreasing bandwidth is that overall correlation values become somewhat higher as bandwidth is decreased. This trend is clear in the 350 Hz centered band results.

To compare the results of the numerical analysis to the recorded data, peak vertical correlation calculations are determined for the precise frequency bands used in the numerical analysis. In each case, bandwidth is varied in an attempt to verify the trend of increasing correlation with decreasing bandwidth indicated by the numerical analysis.

The first of these bands to be reproduced is the set centered at 350 Hz. As in the numerical analysis, bandwidths of 500 Hz, 250 Hz, 125 Hz, and 62.5 Hz are used. The results of this analysis for the first 38g charge are displayed in Figures 31 and 32. As with the two previous sets of smaller frequency bands, this analysis supports the predicted trend of increasing correlation with decreasing bandwidth.

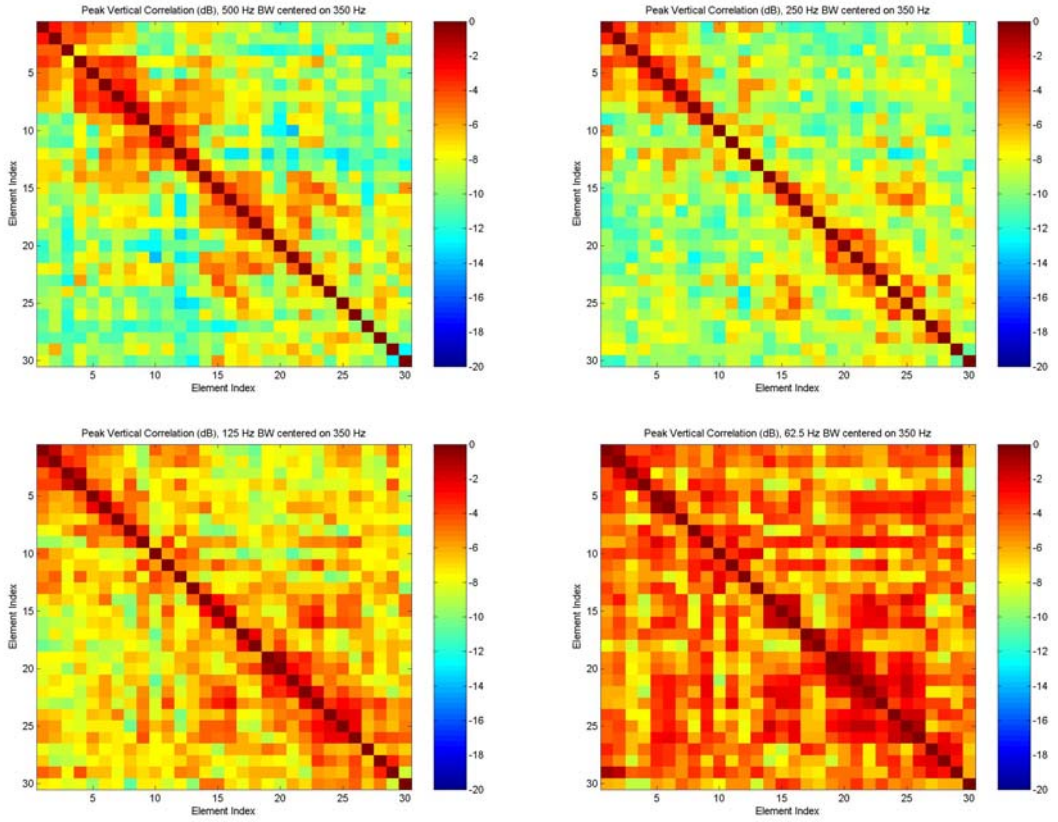

Figure 31. Peak Vertical Correlation Image Plots For 38g Charge, 350 Hz Center Frequency Bands

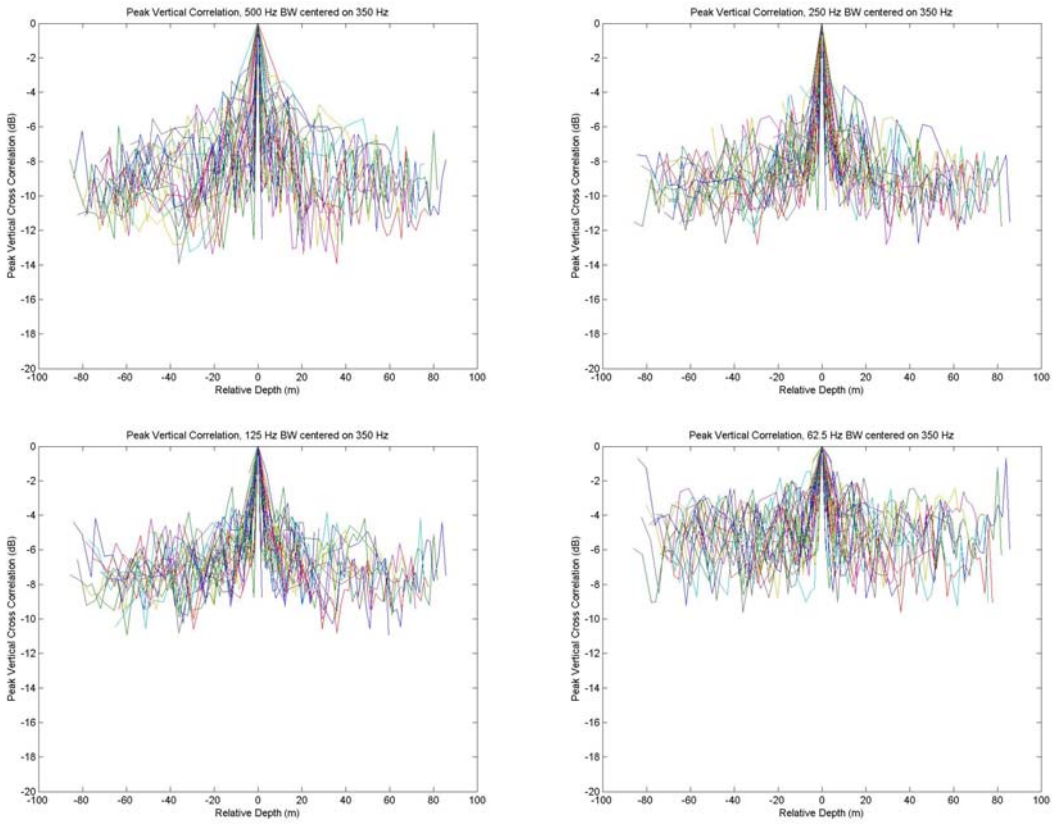

Figure 32. Peak Vertical Correlation Plots For 38g Charge, 350 Hz Center Frequency Bands

The final set of frequency bands to be considered are those centered at 250 Hz. As in the numerical analysis, bandwidths of 250 Hz, 125 Hz, and 62.5 Hz are used. The results of this analysis for the first 38g charge are displayed in Figures 33 and 34. Once again, this analysis supports the predicted trend of increasing correlation with decreasing bandwidth, as does all of the data analysis conducted. Because this trend was consistently more noticeable in the numerical analysis for the volume reverberation, the result of this data analysis may indicate a dominant contribution from the bottom volume fluctuations.

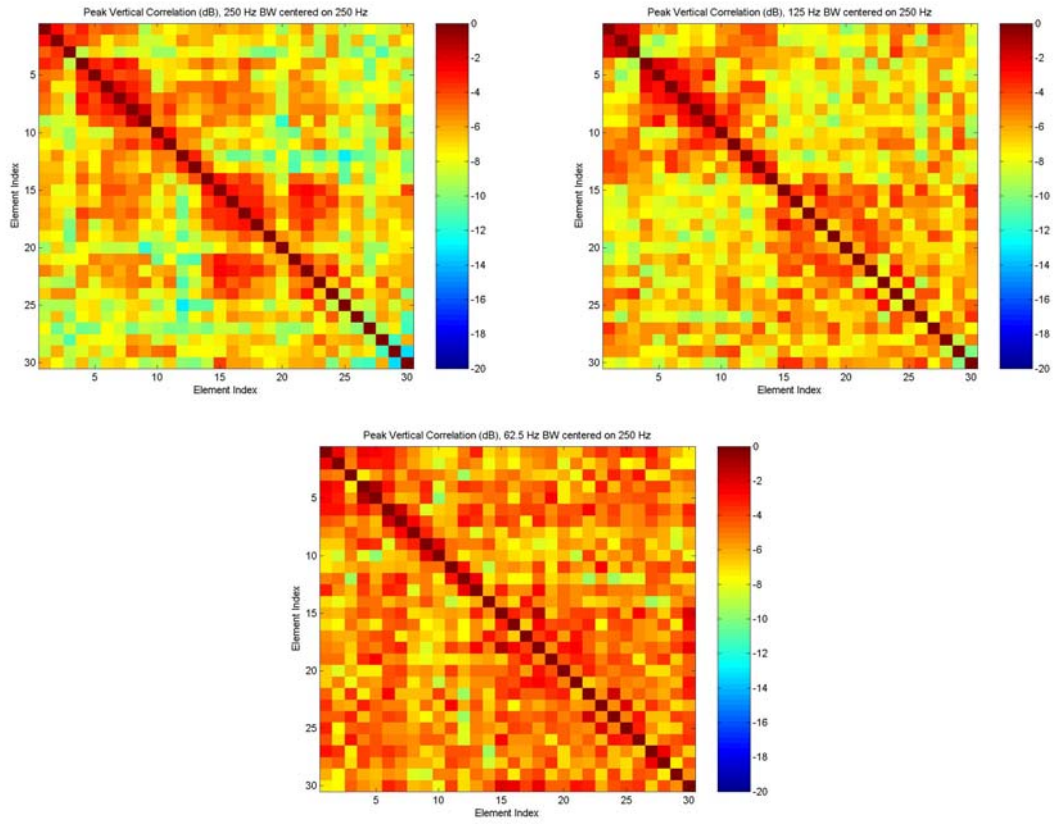

Figure 33. Peak Vertical Correlation Image Plots For 38g Charge, 250 Hz Center Frequency Bands

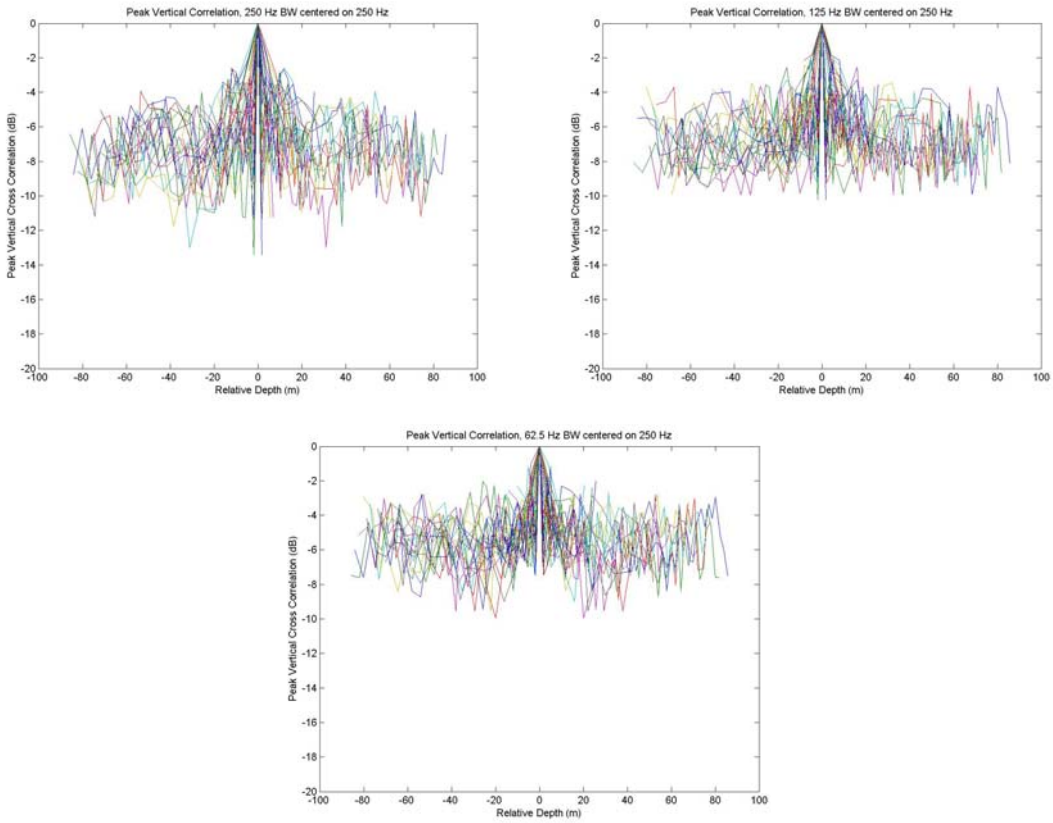

Figure 34. Peak Vertical Correlation Plots For 38g Charge, 250 Hz Center Frequency Bands

THIS PAGE INTENTIONALLY LEFT BLANK

V. SUMMARY

The focus of this thesis was to examine the spatial coherence of broadband reverberation data in a shallow water environment using explosive charges, and determine if unique features of the interface or volume reverberation structure could be used to distinguish the dominant scattering mechanism. To accomplish this, a numerical model was employed to predict the peak vertical correlation structure for the water/bottom interface, the bottom/sub-bottom interface, and the bottom volume over several different bandwidths in this environment. The environment and geometry were chosen to approximate the conditions present during the East China Sea component of ASIAEX and to match the conditions used in previous work as much as practical. Included in this numerical analysis was the incorporation of an explosive SUS charge frequency spectrum, a change from the Hanning window spectrum used in previous work, to better model the explosive sources used in ASIAEX. A larger 500 Hz bandwidth calculated over 1024 frequency bins was also chosen to more accurately simulate a wideband source than the previous 250 Hz bandwidth calculated over 512 frequency bins.

Several environmental parameters were also varied with respect to a set of reference conditions to determine their influence on the peak vertical correlation structure. The environmental variations considered were variations in the degree of roughness for the water/bottom and the bottom/sub-bottom interfaces, variations in the magnitude of bottom volume sound speed perturbations, and variations in the magnitude of water volume sound speed turbulence. These variations in the environment displayed little overall influence on the peak vertical correlation structure. In general, the few variations that were observed were not strong and lacked a clear trend. The one instance where a clear trend was observed was an increase in peak vertical correlation for the largest bottom volume sound speed perturbation. However, this only occurred when given an unrealistic magnitude of the volume perturbation, which resulted in a significant drop in propagation energy, and should not be considered a useful result.

The numerical analysis of the modeled explosive source data determined that no exploitable trend in peak vertical correlation existed with decreasing bandwidth. Peak correlation values from both interfaces appeared roughly equal to those from the bottom volume in all cases. Only an increasing trend in the peak vertical correlation for all three of the contributors was observed. Analysis of the recorded data collected during ASIAEX was consistent with the results of this numerical analysis. In four separate cases, including the 2 cases specifically modeled in the numerical analysis, a decrease in bandwidth resulted in an increase in vertical correlation. However, since no exploitable trend was observed in the numerical analysis to distinguish the reverberation mechanism, no further information regarding interface or volume scattering could be determined from the recorded data.

The previous work suggested that an exploitable trend in peak vertical correlation with decreasing bandwidth does exist for this environment and geometry, at least when a different source spectrum is used. This was confirmed by performing the numerical analysis using the source from the previous work, a 250 Hz bandwidth, 250 Hz center frequency, Hanning windowed source. The peak vertical correlation from both interfaces remained constant with decreasing bandwidth, but peak vertical correlation from the bottom volume increased from levels clearly below that of the interfaces to levels similar to those of the interfaces. This qualifies as an exploitable trend which spatial analysis of recorded signals could leverage to discriminate interface scatter from volume scatter.

Unfortunately, the cause of this difference between a lack of exploitable trend in the current work and its presence in the previous work was determined to be the structure of the source spectrum applied. The various narrow peaks present in the frequency spectrum of an explosive source, such as a SUS, act like several small bandpass filters in the frequency domain. Since the source spectrum already has the same effect as running the signal through several narrow bandpass filters, further bandpass filtration of the signal has little effect and should not be expected to display a trend. As a result, the use of a broadband explosive spectrum was found to be a poor choice for the application of a spatial correlation method to discriminate between interface and bottom volume scattering.

Despite the fact that it did not yield an exploitable trend, the numerical analysis did show that peak vertical correlation structure was altered little by both direct and indirect environmental influences. This suggests that exploitable trends in spatial coherence are robust in the face of environmental variability and that it is the nature of the source spectrum that is the primary discriminating factor in the ability to yield an exploitable trend. It should be noted that in the example provided in Ivakin's work, the observed trend was that interface coherence was lower for the larger pulse length while the volume coherence remained unchanged. The analogous trend with decreasing bandwidth seen in the numerical analysis for a Hanning windowed source showed an opposite trend. The volume coherence was greater for smaller bandwidths (larger pulse lengths) while the interface coherence remained unchanged. However, both still show that the difference between interface and volume coherence was greatest for larger bandwidths (shorter pulse length). The reason for the difference in trend between theory and numerical analysis is unclear, but it should be noted that the results from the recorded data displayed a similar overall trend to the combined trends from the Hanning windowed source analysis, such that the overall vertical coherence increased for smaller bandwidths. Therefore, there is some indication that the volume rather than the interface may dominate reverberation in the measured data, although the use of an explosive spectrum may preclude such a conclusion.

With the conclusion of this thesis, recommendations for future work include an investigation of the effects of both rough sea surface scatter and multiple radial returns. The incorporation of the effects of rough sea surface scatter into the MMPE Model and the investigation of its predicted influence on peak vertical correlation would add the effects of variation in another major environmental component on peak vertical correlation structure to our knowledge base. An investigation of the influence of multiple radial returns on the signal coherence would make this type of analysis even more realistic. Further work could also be performed to determine the discrepancy between the theoretically predicted influence of bandwidth and the observed trends in the numerical analysis.

If further analysis supports the conclusion that volume scatter dominates the ASIAEX reverberation data, then it may be possible to combine measured and modeled

results to invert for the volume scattering strength, S_v. Evaluation of this could then lead to an estimate of the volume perturbation spectral strength, which could be compared to results obtained from bottom core samples taken from the region. Furthermore, such a successful discrimination of the volume reverberation from active, broadband returns could be exploited in future processing algorithms to aid in the detection of other scattering targets of interest.

LIST OF REFERENCES

[1] Makris, N.C. and Berkson, J.M. "Long-range backscatter from the Mid-Atlantic Ridge," *J. Acoust. Soc. Am.*, **95**, pp. 1865-1881, 1994.

[2] Smith, K.B., and Lit-Siew, L. "Broadband Parabolic Equation Modeling of Acoustic Bottom Interface and Volume Reverberation in Shallow Water," Proceedings of 5th European Conference on Underwater Acoustics, Lyon, France, 10-13 July, pp. 1171-1176, 2000.

[3] Smith, K.B., Hodgkiss, W.S., and Tappert, F.D. "Propagation and analysis issues in the prediction of long-range reverberation," *J. Acoust. Soc. Am.*, **99**, pp. 1387-1404, 1996.

[4] Smith, K.B. and Cushman, E.B. "A comparison of quasi-continuous wave and broadband travel time techniques in the prediction of long-range reverberation," *J. Acoust. Soc. Am*., **102**, pp. 2063-2071, 1997.

[5] Li, L.S. "Parabolic Equation Modeling of Bottom Interface and Volume Reverberation in Shallow Water," Master's Thesis, Naval Postgraduate School, Monterey, CA, September 2000.

[6] Kao, H. "Numerical Analysis of Bottom Reverberation and Influence of Density Fluctuations," Master's Thesis, Naval Postgraduate School, Monterey, CA, December 2001.

[7] Lee, B.-C. "Environmental Influence on Shallow Water Bottom Reverberation," *Master's Thesis, Naval Postgraduate School*, Monterey, CA, March 2002.

[8] Smith, K.B. "Convergence, stability, and variability of shallow water acoustic predictions using a split-step Fourier parabolic equation model," *J. Comp. Acoust.*, **9**, pp. 243-285, 2000.

[9] Tappert, F.D. The parabolic approximation method (Chapter V). *Lecture Notes in Physics*, **70**, Wave Propagation and Underwater Acoustics, eds. J.B. Keller and J.S. Papadakis, Springer-Verlag, New York, 1977.

[10] Hardin, R.H. and Tappert, F.D. "Applications of the split-step Fourier method to the numerical solution of nonlinear and variable coefficient wave equations," *SIAM Rev*., **15**, pg. 423, 1973.

[11] Goff, J.A. and Jordan, T.H. "Stochastic modeling of seafloor morphology: Inversion of Sea Beam data for second-order statistics," *J. Geophys. Res*., **93**, pp. 13589-13609, 1988.

[12] Yamamoto, T. "Velocity variabilities and other physical properties of marine sediments measured by crosswell acoustic tomography," *J. Acoust. Soc. Am*., **98**, pp. 2235-2248, 1995.

[13] Ivakin, A.N. "Models of scattering for remote acoustic sensing of the seafloor," *Acoustical Oceanography*, Proc. Institute of Acoustics, **23**, eds. T.G. Leighton, G.J. Heald, H.D. Griffiths, G. Griffiths, pp. 265-275, 2001.

[14] Tatarski, V.I. *Wave Propagation in a Turbulent Medium* (Dover Publications, 1961)

[15] Henyey, F.S., Rouseff, D., Grochocinski, J.M., Reynolds, S.A., Williams, K.L., and Ewart, T.E. "Effects of Internal Waves and Turbulence on a Horizontal Aperture Sonar," *IEEE Journal of Oceanic Engineering*, Volume 22, Number 2, pp. 270-280, 1997.

[16] Duda, T.F. and Trivett, D.A. "Predicted scattering of sound by diffuse hydrothermal vent plumes at mid-ocean ridges," *J. Acoust. Soc. Am.* Volume 103 (1), pp.330-335, 1998.

[17] Duda, T.F., Flatte', S.M., and Creamer, D.B. "Modelling Meter-Scale Acoustic Intensity Fluctuations From Oceanic Fine Structure and Microstructure," *Journal of Geophysical Research*. Volume 93, Number C5, pp.5130-5142, 1988

[18] Duda, T.F. "Modeling Weak Fluctuations of Undersea Telemetry Signals," *IEEE Journal of Oceanic Engineering*, Volume 16, Number 1, pp.3-11, 1991

[19] Smith, K.B., Li, L.-S., Lee, B.-C., and Kao, H., "Sediment interface and volume reverberation modeling with the parabolic approximation," *Proceedings of the Third International Conference on Modeling and Experimental Measurements in Acoustics*, Cadiz, Spain, 16-18 June, pp. 277-296, 2003.

THIS PAGE INTENTIONALLY LEFT BLANK

INITIAL DISTRIBUTION LIST

1. Defense Technical Information Center
   Ft. Belvoir, Virginia

2. Dudley Knox Library
   Naval Postgraduate School
   Monterey, California

3. Dr. Ellen Livingston (Code 3210A)
   Office of Naval Research
   Arlington, Virginia

4. Prof. Kevin B. Smith (Code PH/Sk)
   Department of Physics
   Naval Postgraduate School
   Monterey, California

5. Dr. Peter H. Dahl
   Applied Physics Laboratory
   University of Washington
   Seattle, Washington

6. Prof. James H. Miller
   Department of Ocean Engineering
   University of Rhode Island
   Narragansett Bay, Rhode Island

7. Prof. Ji-Xun Zhou
   Georgia Institute of Technology
   Atlanta, Georgia

8. Dr. David P. Knobles
   Applied Research Laboratory
   Austin, Texas